Universidad de Concepción
Dirección de Postgrado
Facultad de Ingeniería -Programa de Magister en Ciencias de la Ingeniería con mención en Ingeniería Mecánica

Análisis de la distribución del peso de la cúpula sobre los mecanismos de rotación del Very Large Telescope ubicado en el Observatorio Paranal, y desarrollo de un método de monitoreo de condición.

("Analysis of the load distribution of the dome weight on the rotation mechanisms of the Very Large Telescope located at the Paranal Observatory, and development of a condition monitoring method.")

Tesis para optar al grado de Magister en Ciencias de la Ingeniería con mención en Ingeniería Mecánica

SABINA MARIA RAYO RAMÍREZ

CONCEPCIÓN-CHILE

2020

Profesor Guía: Dr.-Ing. Cristián Molina Vicuña
Dpto. de Ingeniería Mecánica, Facultad de Ingeniería
Universidad de Concepción

ABSTRACT

The Very Large Telescope (VLT) has a set of rotation mechanisms allowing the positioning of the dome for night observations. The rotation mechanism (RTM) is a critical equipment, because a failure significantly affects the astronomic observation time. During recent years, the fixed bearings of the vertical wheels of the RTMs have been experiencing damage. Slight misalignments of the bogies can induce significant axial forces when the bogie wheel suddenly slips to release the strain energy (stick-slip effect). This energy is built up when the wheel tracks off of the desired circular path. The stick-slip effect depends on the friction force, and thus on the normal force (that means dome weight divided by number of RTM wheels). Therefore, a normal force higher than the nominal, that means an unequal distribution of the dome weight on the bogies, could cause an excessive axial thrust damaging the bearings.

Accordingly, the first general objective of this work is the development of a method to determine the static load distribution of the dome weight on the RTM of the VLT. The associated specific objectives are the selection of the measurement method and signal processing tools for determining the actual load distribution, as well as the estimation of the actual load supported by each vertical wheel.

The method consists in using Fujifilm´s Prescale measurement films which permit the obtainment of images of the contact pressure and its distribution between the wheel and the rail. The images were processed by a software program written in Python and the results revealed that some RTMs present an important underload up to 32% less than considered by design. Contrary, neighboring RTMs compensate this situation by supporting an overload up to 43% higher compared to the nominal load.

The results lead to the conclusion that unequal load distribution of the dome weight on the RTMs exists. Furthermore, the minimum axial force which is released when the wheel of a RTM with normal load suddenly slips already exceed the maximum permissible axial load of the bearings of the RTMs. Therefore, it can be concluded that the stick-slip effect already per se contributes to excessive axial thrust, which can damage the bearings of the RTMs.

From the fact that it is difficult to avoid any bogie misalignment the second general objective of this work arises, which consists in the development of a RTM condition monitoring method. The associated specific objectives are the identification of measurement variables potentially suitable for the condition monitoring of the RTMs, field measurements of the selected variables in different RTM units and the analysis of the measured data as well as the evaluation of results.

The RTM wheel shaft has a very slow rotational speed which makes it difficult to monitor the bearings because of the generation of low impact energy due to the relative motion of the components when defects are present. Four RTMs were selected for the measurements. One which had been replaced three months before, and three which have never been changed since telescope´s first light. The recently replaced RTM was selected as a reference of defect-free condition. For the analysis of the bearing condition, acoustic emission (AE), acceleration vibration and displacement vibration of the shaft were measured. The signals were processed using time- and frequency-domain based techniques such as enveloping method and spectral kurtosis.

An incipient bearing failure of the outer race of the RTM could be identified by the AE measurements, whereas acceleration and displacement vibration did not provide any signs of defect. These results lead to the conclusion that the AE analysis can detect incipient defects even in slow-speed bearings, whereas

acceleration and shaft displacement vibration measurements are not as suitable for the detection of early stage bearing failure in the RTMs.

RESUMEN

El mecanismo de rotación (RTM), o bogie, es el equipo que permite que la cúpula del Very Large Telescope (VLT) pueda girar para las observaciones durante la noche. Es un equipo crítico dado que una falla puede afectar de forma significativa el tiempo de observación astronómica. Durante los últimos años, los rodamientos fijos de las ruedas verticales de los RTMs están sufriendo daño. Pequeños desalineamientos de los bogies pueden inducir fuerzas axiales significativas cuando la rueda del bogie de repente resbala para liberar la energía de deformación (efecto "stick-slip"). Esta energía se acumula cuando la rueda sale de la trayectoria circular. El efecto "stick-slip" depende de la fuerza de fricción, y de esta manera de la fuerza normal (es decir del peso de la cúpula dividido por la cantidad de ruedas de los mecanismos de rotación). Por lo tanto, una fuerza normal mayor a la nominal, es decir una distribución desigual del peso de la cúpula encima de los bogies, podría causar una fuerza axial excesivamente alta, la cual puede dañar los rodamientos.

En consecuencia, el primer objetivo general de este trabajo es el desarrollo de una metodología para determinar la distribución estática del peso de la cúpula sobre los mecanismos de rotación del VLT. Los objetivos específicos asociados consisten en la selección de un método de medición y la forma de procesamiento de señales para determinar la distribución actual del peso, como también la estimación de la carga actual que soporta cada rueda vertical.

El método consiste en el uso de películas Fujifilm´s Prescale, que permiten la obtención de imágenes de la presión de contacto y su distribución entre la rueda y el riel. Las imágenes fueron analizadas con un programa de software escrito en Python, y los resultados mostraron que algunos RTMs presentan una importante subcarga hasta un 32% menor en comparación con el valor considerado por diseño. Por otro lado, RTMs adyacentes compensan esta situación soportando una sobrecarga hasta un 43% más alto en comparación con el valor nominal.

Estos resultados permiten concluir que existe una distribución desigual del peso de la cúpula encima de los mecanismos de rotación. Además, la fuerza mínima que es liberada cuando una rueda del RTM con una carga normal resbala ya supera la máxima carga axial admisible con respecto a los rodamientos de los RTMs. Es por eso que se puede concluir que el efecto "stick-slip" de por sí ya contribuye a la presencia de fuerzas axiales excesivamente altas, que pueden dañar los rodamientos de los RTMs.

Dado que es difícil evitar cualquier desalineamiento del bogie, el segundo objetivo general de este trabajo consiste en el desarrollo de una estrategia de monitoreo de condición. Los objetivos específicos asociados son la identificación de variables medibles que potencialmente son aptos para el monitoreo de condición de los RTMs, mediciones in situ de las variables elegidas considerando RTMs diferentes, y el análisis de los datos como también una evaluación de los resultados.

El eje de la rueda de los RTMs tiene una velocidad de rotación muy lenta lo cual dificulta el monitoreo de los rodamientos. La razón es que se genera solamente una baja energía de impacto debido al movimiento relativo de las componentes si un defecto existe. Se eligieron cuatro RTMs para las mediciones. Uno que fue reemplazado 3 meses antes de las mediciones, y tres que nunca fueron cambiados desde los telescopios vieron su primera luz. Analizando los rodamientos de lado interior como también del exterior emisiones acústicas (AE), aceleración vibratoria y el desplazamiento vibratorio del eje fueron medidos, y las señales procesadas usando técnicas basadas en el dominio de tiempo y frecuencia como el método de la envolvente y la curtosis espectral.

Se pudo identificar un defecto incipiente en la pista externa de un rodamiento de un RTM a través de las mediciones de las AE. Aceleración vibratoria y el desplazamiento vibratorio del eje no pudieron demonstrar alguna falla. Es por eso que se puede concluir que el análisis de las AE puede detectar un defecto incipiente incluso en rodamientos lentos, mientras las mediciones de la aceleración vibratoria y del desplazamiento vibratorio del eje no son tan aptas para la detección de una falla en etapa temprana en los rodamientos de los RTMs.

CONTENTS

LIST OF FIGURES

LIST OF TABLES

LIST OF SYMBOLS

B	Bearing width [mm]
d	Bearing bore diameter [mm]
F	Force [N]
f	frequency [Hz]
N	Normal force [N]
μ	Coefficient of friction [-]
z	Number of gear teeth [-]
Δ	Delta [-]

SUBSCRIPTS

a	axial
g	gear mesh
p	permissible
f	friction

ACRONYMS

ACC	Acceleration
AE	Acoustic Emission
AZ	Arizona
BPFI	Ball Pass Frequency Of Inner Race
BPFO	Ball Pass Frequency Of Outer Race
BSF	Ball Spin Frequency
C	Idle
CDF	Characteristic Defect Frequencies
DFT	Discrete Fourier Transform
ELT	Extremely Large Telescope

ESO	European Southern Observatory
FFT	Fast Fourier Transform
FS	Sampling Frequency
FTF	Fundamental Train Frequency
H	Horizontal
HFRT	High Frequency Resonance Technique
LBT	Large Binocular Telescope
LG	Lateral Guide Wheel
M	Motor driven
RPM	Revolutions Per Minute
RTM	Rotation Mechanism
SK	Spectral Kurtosis
V	Vertical
VLT	Very Large Telescope
UT	Unit Telescope

CHAPTER 1

Introduction

1.1 Problem description

Paranal is the home of the European Southern Observatory (ESO) Very Large Telescope (VLT), located 120 km south of the city of Antofagasta in the Chilean Atacama desert. The VLT consists of four individual optical telescopes, each of them enclosed in a building called enclosure. The main function of the enclosure in the closed position is to protect the telescope and its instrumentation, as well as to preserve the thermal environment. In the open position, it has to allow the telescope a free field of view by means of a large slit in the dome. This can be seen in Figure 1.

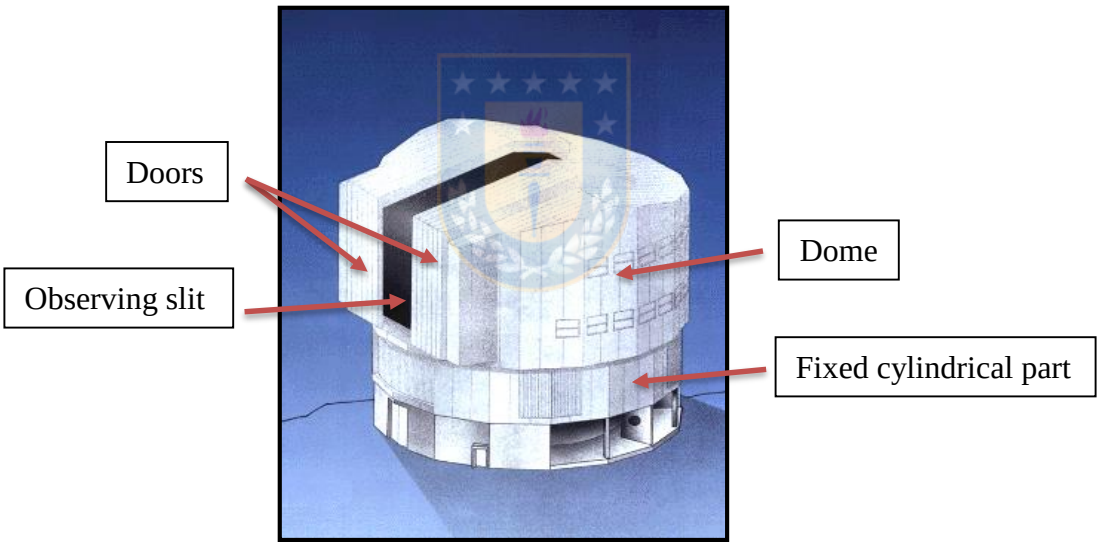

Figure 1. Enclosure of the VLT Unit Telescope (UT) (source: [Bugueno 2016]).

The enclosure consists of a fixed cylindrical part and an upper rotating part called the dome. Two doors can close the observing slit.

The set of units allowing the rotation of the dome for night observations is called rotation mechanism (RTM) or bogies. The RTM consists in 8 bogies assemblies mounted to the lower (fixed) portion of the enclosure, each using two vertical wheels, one driven and one idle wheel. There are lateral guides between the vertical wheels constraining enclosure motion in radial direction. The rail is composed of built-up box-beams and machined running surfaces. Figure 2 and 3 show the bogie assembly.

Figure 2. Bogie with the two vertical wheels.

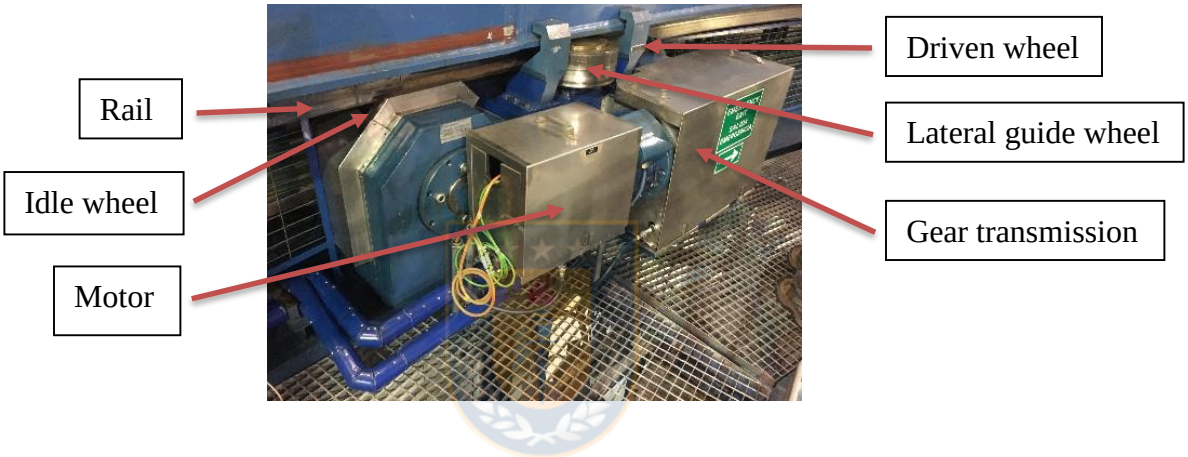

Figure 3. Bogie assembly.

During recent years mechanical parts of the RTMs have been suffering damage, in particular the fixed bearings of the vertical wheels. For example, in September 2015 the RTM5 of the UT4 showed a high quantity of metallic particles during oil exchange in the drive wheel. The unit was removed and checked, presenting clear damage in the outer race of the gear box side (fixed) bearing, which is shown in Figure 4.

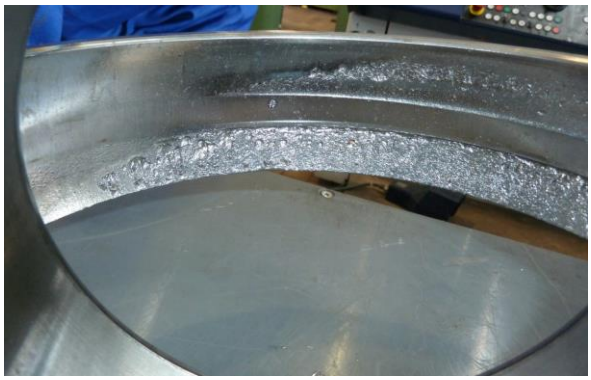

Figure 4. Damage in the outer race of the bearing, UT4-RTM 5(source: [Palacio 2015]).

Closer inspection of the damaged zone revealed signs of pitting, which is the most typical fatigue failure in bearings. Additionally, the damaged area is loaded to one side, which implies the possibility of the presence of important axial thrust or misalignment of the wheels.

In September 2017 there was a catastrophic failure of RTM2 of the UT4 due to bearing damage (gear box side) of the idle wheel, which can be observed in Figure 5. The RTM had to be dismounted and replaced.

Figure 5. Bearing damage, UT4-RTM 2 (source: [ESO Workshop Paranal 2017]).

Literature research shows that other observatories describe similar problems with the bearings of the enclosure rotation system. [Howard 2012] reviewed the system design and current performance of the Large Binocular Telescope (LBT) in Tucson, AZ, USA, because of the failure of several wheel bearings. The rotating enclosure of the LBT is a structure supported by 4 bogies with a total of 20 wheels. The identified deficiencies were mainly low wheel bearing capacity, bogie misalignment and excessive rail loading due to the dome weight. A survey of the rotation system of 11 optical, infrared and submillimeter 3-15 m telescope enclosures shows also that the bogie misalignment and the consequent stick-slip effect is a common problem [Bigelow 2016].

The stick-slip effect refers to a build-up of strain energy due to slight misalignments which is released when the friction force (F_f) at the wheel/rail contact patch is exceeded, and the bogie wheel suddenly slips to release the strain energy. This effect induces significant axial forces, which could be the cause for the bearing failures. The upper limit of the friction force F_f is defined as:

$$F_f = N \cdot \mu \tag{1}$$

where N is the normal force and μ the coefficient of friction. If for some reason an increase of the normal force in one or more contacts occurs, the upper limit of F_f increases according to (1) and a higher axial thrust on the wheel shaft is expected in case of the stick-slip effect. Theoretically the normal force is equal to the dome weight divided by the number of wheels, but in light of this possible situation it is important to know the real load distribution of the dome weight on the RTMs.

1.2 Motivation

As can be inferred from the problem description, the RTM is a critical equipment. The damage of the fixed bearings of the vertical wheels, which appeared during recent years in the VLT, provoked an important downtime for repair, affecting astronomic observation time. Furthermore, several observatories present similar problems [Howard 2012, Bigelow 2016], and it seems that small misalignments with consequent significant axial forces could be the cause for these problems.

Additionally, the Extremely Large Telescope (ELT) is under construction on the Cerro Armazones in Chile. This telescope will be the largest optical/near-infrared telescope in the world. In the preliminary design the enclosure rotation mechanism will be quite similar in comparison with the VLT [Murga 2008], but the bogies will carry structures that are 2-3 times larger in diameter and much heavier than the enclosures for the previous generation telescopes.

As the axial thrust is associated with the normal force, the analysis of the load distribution of the dome weight on the RTM could clarify the failure origin of the bearings, and so contribute to prevent future important downtime of the VLT. Further, it could provide the possibility to consider key design features for the development of the RTMs for the ELT enclosure.

To avoid unexpected and/or catastrophic failure of the RTMs a condition monitoring method of the RTMs should be developed due to the possibility to identify bearing defects during an early stage.

1.3 Hypotheses and objectives

1.3.1 Hypotheses

The hypotheses (H) are:

H1. Bearing damage of the VLT rotation mechanisms is caused by unequal load distribution of the dome weight on the RTM wheels.

H2. The development of a RTM condition monitoring method can detect defects in the RTM bearings, thus avoiding unexpected and/or catastrophic failures.

1.3.2 General objectives

The general objectives (GO) are:

GO1. Design of a method to determine the static load distribution of the dome weight on the RTM of the VLT.

GO2. Development of a RTM condition monitoring method.

1.3.3 Specific objectives

The specific objectives (SO) are:

SO1. Selection of the measurement method and signal processing tools for determining the actual load distribution of the dome weight on the RTM.

SO2. Estimation of the actual load supported by each vertical wheel.

SO4. Identification of measurement variables potentially suitable for the condition monitoring of the RTMs.

SO5. Field measurements of the selected variables in different RTM units.

SO6. Analysis of measured data and evaluation of results.

1.4 Structure of the work

This work is structured in the following manner:

Chapter 2 – Describes the design of the VLT enclosure rotation system in detail.

Chapter 3 – Presents a method to determine the static load distribution of the dome weight on the RTM of the VLT and discusses results of the measurements.

Chapter 4 – Describes different measurement variables which can be useful in the detection of a bearing defect in an early stage.

Chapter 5 – Details the measurement setup used for the condition monitoring measurement campaign.

Chapter 6 – Describes different signal processing techniques used.

Chapter 7 – Shows and discuss the condition monitoring measurement results.

Chapter 8 – Presents conclusions and perspectives for future work.

CHAPTER 2

Design of the VLT enclosure rotation system

2.1 Design description of the VLT enclosure rotation system

Figure 6 shows that the VLT enclosure is supported on 8 bogies (RTM1 – RTM8) assemblies, each using two wheels which are slightly conical (1.13°). The wheel orientation is vertical and accordingly slightly inclined (1.13°) [Dome Bogies Workshop 2016]. The diameter of the wheels is 0.6 m and the width 0.125 m.

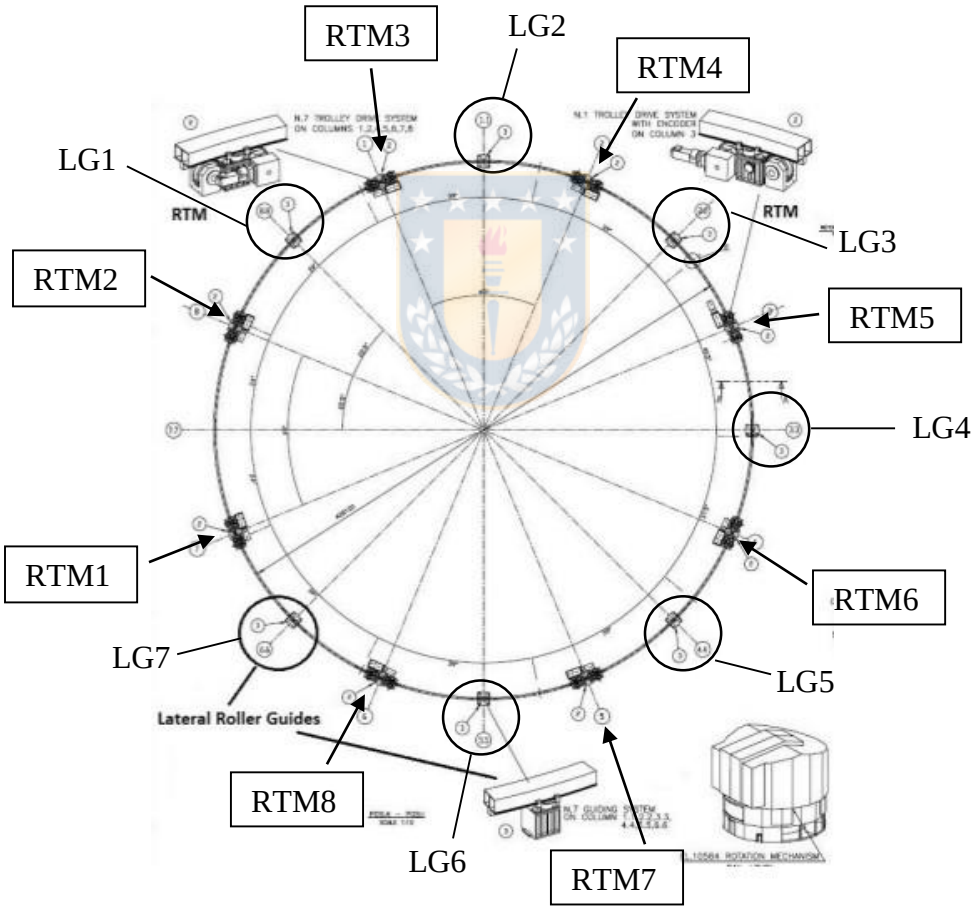

Figure 6. Design of the VLT enclosure rotating system in UT1 (source: [SEBIS-1 1994]).

The VLT enclosure design is unusual because the bogies are mounted to the lower (fixed) portion of the enclosure and not to the upper moving portion. Fixed bogies appear to be used in case of relatively stiff and light-weight enclosures with uniform azimuthal load distribution. So cyclically-varying loads on the

bogie assemblies due to rotation of the enclosure are limited [Bigelow 2016]. Theoretically each of the 16 wheels carries an average load of 17.5 tons.

There are two types of lateral guide wheels operating with rollers on the inboard and outboard sides of the rail section. 8 pairs of the first type are located between the vertical wheels on the main bogies assemblies. Additionally, 7 pairs of the second type are mounted independently from the main bogies and spaced equally between them. This can be seen in Figure 6, where the lateral guide wheels of the second type are marked with “LG”. The lateral guide system constrains enclosure motion in the radial direction.

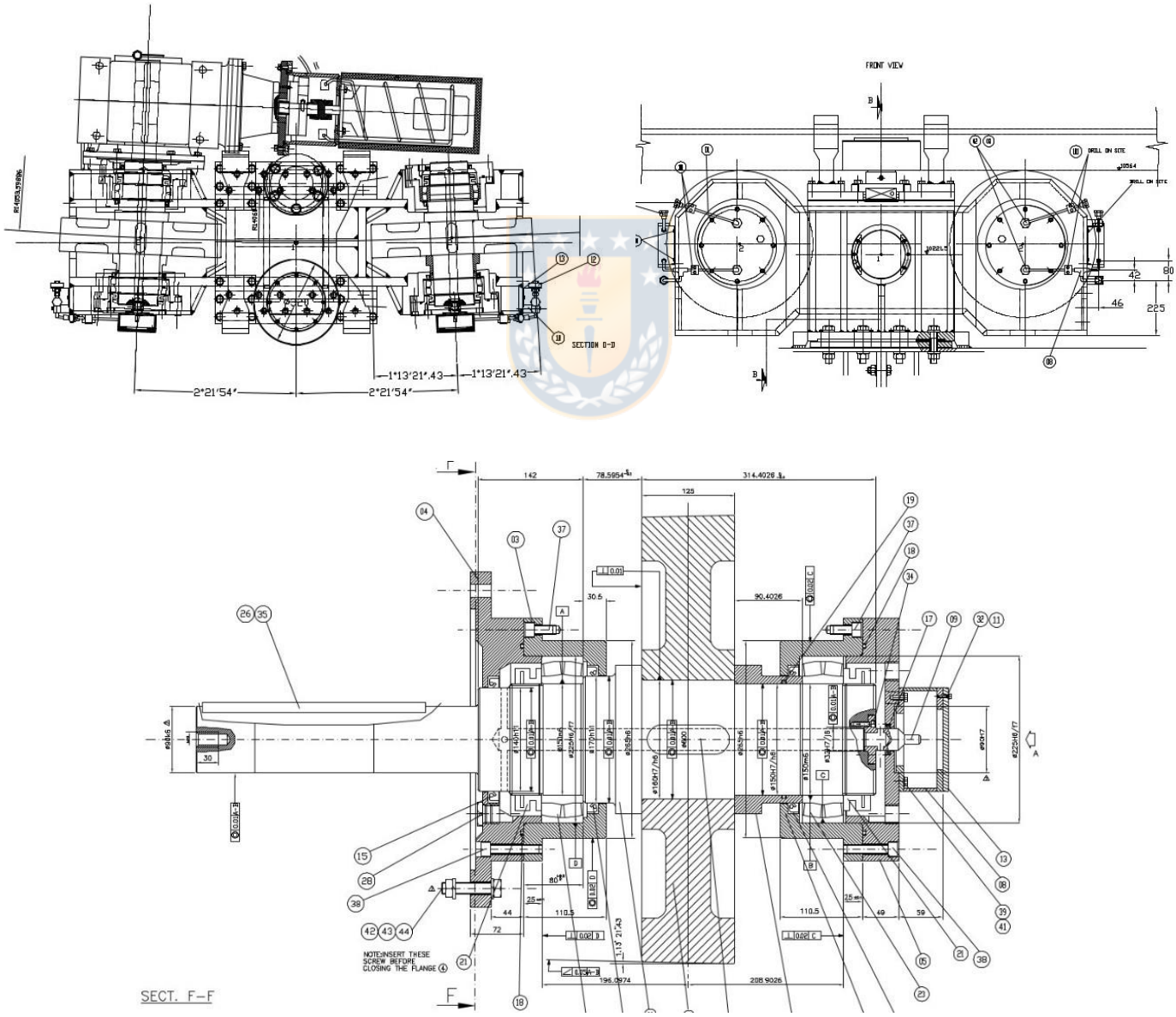

Figure 7. Bogie assembly (source: [SEBIS-2, SEBIS-3 1994]).

The vertical wheels articulate on an elastomeric pad, which allows the bogie assembly to balance loads between the two wheels and provide some vertical and tilting compliance. Each bogie assembly includes one driven and one idle wheel. The drive system has a motor and gearbox, which are directly coupled to the drive wheels. SKF spherical roller bearings are used. All this is shown in Figure 7.

The rail is composed of built-up box-beams and machined running surfaces for the vertical wheels and the lateral guide wheels. The track joints are bolted and the track/wheel interface is not lubricated.

The maximum speed of the enclosure is 2 °/s [SEBIS-4 1994], which means a rotational speed of the RTM wheel shaft of approximately 15 RPM.

CHAPTER 3

Analysis of the load distribution of the dome weight on the RTM

3.1 Introduction

In [Rayo 2019] the use of Fujifilm´s Prescale pressure measurement films is proposed for the analysis of the load distribution of the dome weight on the RTM. The films reveal the required information by measuring the contact pressure of the dome weight on the RTM and its distribution. Applied pressure differences between the vertical wheels and the rail are indicated as red color density variations, as shown in Figure 8.

Figure 8. Fujifilm's Prescale pressure measurement film (source: [https://www.fujifilm.com]).

3.2 Results of the load distribution measurements

In [Rayo 2019] measurements in UT1 and UT4 were performed considering in each case 8 different positions of the enclosure. The enclosure was rotated clockwise and each 45° the measurements were carried out. The results of the dome weight distribution were obtained by a software program written in Python which processed the images. In this section the most important results presented in [Rayo 2019] are shown.

Considering the 8 positions of the enclosure in UT1, Table 1 shows the average load carried by each wheel and the corresponding percentage with reference to the nominal load of 17.5 tons. The number of RTM is indicated, and acronym "M" is used for the motor driven wheel and "C" for the idle wheel. In Figure 9 the same average load information can be observed graphically. The bars of the histogram are marked in red in case of wheels with a 25% higher or lower load, and a reference line at 17.5 tons is drawn. Table 2 shows the error between the total load obtained by the measurements and the total nominal load.

Table 1. Average load of UT1.

RTM	F [tons]	Percentage of nominal load
1M	14.4	82.3
1C	14.4	82.3
2M	19.4	110.9
2C	18.9	108
3M	15.9	90.9
3C	16.4	93.7
4M	25.1	143.4
4C	24.9	142.3
5M	16.1	92
5C	16.5	94.3
6M	19.4	110.9
6V	19.4	110.9
7M	14.1	80.6
7C	13.4	76.6
8M	18.5	105.7
8C	17.8	101.7

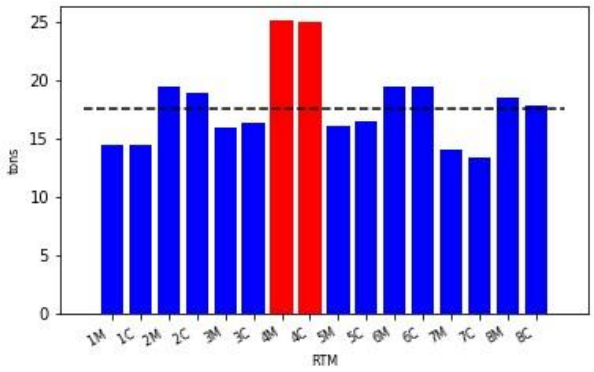

Figure 9. Average load of UT1.

Table 2. Error between total measured load and total nominal load (UT1).

Total nominal load [tons]	Total measured load [tons]	Error [%]
280	284.6	1.6

Analyzing the average load of the UT1, there are four wheels which present an important underload: RTM 1M, 1C, 7M and 7C. Low force on the RTMs per se not is a problem, but it is the reason why neighboring RTMs have to compensate this situation supporting an overload how it can be observed in Figure 9. Especially the RTM 4 presents an important overload over 40%. And this overload contributes to excessive axial thrust by the stick-slip effect as explained in section 1.1, which can damage the bearings of the RTMs.

Adding all the calculated average loads of the wheels of the UT1, the total sum is 284.6 tons in comparison with the nominal load of 280 tons. That means a very low measurement error of only 1.6%.

In the following the results of the UT4 are shown. Considering again the 8 positions of the enclosure, Table 3 shows the average load which carries each wheel of the UT4 and the corresponding percentage of the nominal load of 17.5 tons. In Figure 10 the same average load information can be observed graphically and Table 4 shows the error between the total load obtained by the measurements in the UT4 and the total nominal load. Observing the average load in Figure 10, there are four wheels which present an important underload (wheels 1M, 1C, 3M and 3C), and neighboring RTMs compensating this situation by supporting an overload, in this case up to 15%.

Adding again all the calculated average loads of the wheels of the UT4, the total sum is 275.4 tons in comparison with the nominal load of 280 tons as shown in Table 4. That means once more a low measurement error of only 1.7%.

Table 3. Average load of UT4.

RTM	F [tons]	Percentage of nominal load
1M	12	68.6
1C	13.2	75.4
2M	19.1	109.1
2C	20.3	116
3M	12.9	73.7
3C	14.7	84
4M	20.2	115.4
4C	20.2	115.4
5M	19.4	110.9
5C	15.9	90.9
6M	18.3	104.6
6V	18.6	106.3
7M	16	91.4
7C	17.1	97.7
8M	18.9	108
8C	18.6	106.3

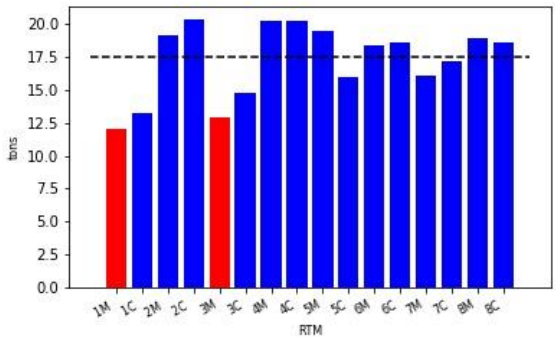

Figure 10. Average load of UT4.

Table 4. Error between total measured load and total nominal load (UT4).

Total nominal load [tons]	Total measured load [tons]	Error [%]
280 tons	275.4 tons	1.7%

3.3 Estimation of the maximum allowed friction force involved in the stick-slip effect according to the maximum permissible axial load of the bearings

As explained in section 1.1 the stick-slip effect refers to a build-up of strain energy due to slight bogie misalignments which is released when the friction force F_f at the wheel/rail contact patch is exceeded, and the bogie wheel suddenly slips to release the strain energy. Therefore, the minimum of the axial thrust caused on the wheel shaft of the RTMs correspond to the F_f.

The bearings used in the RTMs are SKF spherical roller bearings 23030 CC/W33. According to [www.skf.com] the maximum permissible axial load (F_{ap}) in kN can be estimated approximately as shown:

$$F_{ap} = 0.003 \cdot B \cdot d \tag{2}$$

where B is the bearing width and d the bearing bore diameter, both variables indicated in mm. As for the used bearing B = 56mm and d =150 mm, the resulting F_{ap}= 25.2 kN = 2.6 tons.

According to equation (1) the F_f depends on μ and N, where N theoretically is equal to the dome weight divided by the number of wheels, that means N = 17.5 tons. Considering dry and clean steel, according to [www.engineeringtoolbox.com] a kinetic friction coefficient μ of 0.42 is used for calculations. For avoiding a damage of the bearings by the stick slip effect, the limit condition would be $F_f = F_{ap}$. This corresponds to a normal force on the wheels of N = 6.2 tons. That means that the released axial force by the stick-slip effect under normal conditions already can damage the bearings. Considering the maximum average load on the RTM of 25 tons which was obtained by the measurements in the UT1 for the RTM 4 as shown in section 3.2, a suddenly slip of these wheels would release an axial force 4 times higher than permitted.

CHAPTER 4

Description of useful measurement variables for the detection of an early bearing defect

4.1 Introduction

The analysis of the load distribution in chapter 3 has shown that the load distribution of the dome weight on the RTMs is unequal. Furthermore, the minimum axial force which is released when the wheel of a RTM with normal load suddenly slips already exceed the maximum permissible axial load of the bearings of the RTMs. For this reason, the need to develop a condition monitoring method of the RTMs arises to identify bearing defects during an early stage, thus avoiding an unexpected and/or catastrophic failure.

As mentioned in section 2.2 the maximum speed of the VLT enclosure is 2 °/s [SEBIS-4 1994], which means a rotational speed of the RTM wheel shaft of 15 RPM approximately. Slow-speed bearings are commonly defined as bearings rotating at a speed between 100 and 600 RPM, whereas very slow-speed bearings are those rotating below 100 RPM [Saavedra 2005]. The challenge in monitoring very slow-speed bearings is that the contact between defective components generates low impact energy making the symptoms of the defect difficult to detect. This chapter describes which measurement variables were selected, their features and the reason why they could be useful in the early bearing fault detection.

4.2 Bearing failure stages

A bearing fault usually develops in different stages, and consequently that affects the diagnostic procedure. A bearing defect can be categorized in four stages depending on the size of the defect [Saavedra 2005].

At the first stage the defect starts frequently as a crack developing below the surface of the material. As the rolling elements pass over the defect, encouraging the crack to develop, the bearing material is excited and ultrasonic waves are produced. In this stage a bearing defect can be identified only by techniques that work efficiently at high frequency regions, that means over 20 kHz. On example for such a technique is the acoustic emission (AE) analysis.

As the defect develops, and the bearing´s structural integrity is compromised, impacts are produced when the ball passes over the defect. If the impacts excite bearing or sensor natural frequency (generally between 1 kHz and 5 kHz) the energy level starts to increase. In this case the envelope analysis, which is explained in section 4.4, and a high frequency acceleration (ACC) spectrum can pinpoint the bearing fault. A low frequency velocity spectrum will still not show clear evidence.

At the third stage of a bearing fault the most commonly recognizable patterns can be measured at low frequency spectrum. Despite the fact that high frequency energy continues and envelope analysis is still efficient, the classic patterns of bearing failure are now present at velocity spectrum.

At the final stage of a bearing defect a significant damage is present. The vibration spectrum noise floor will start to raise and it is almost impossible to detect the characteristic frequencies of the bearing defects. Machines with bearings in final stage should not be operated as a catastrophic failure can be imminent.

This typical bearing fault development in stages can be observed graphically in Figure 11.

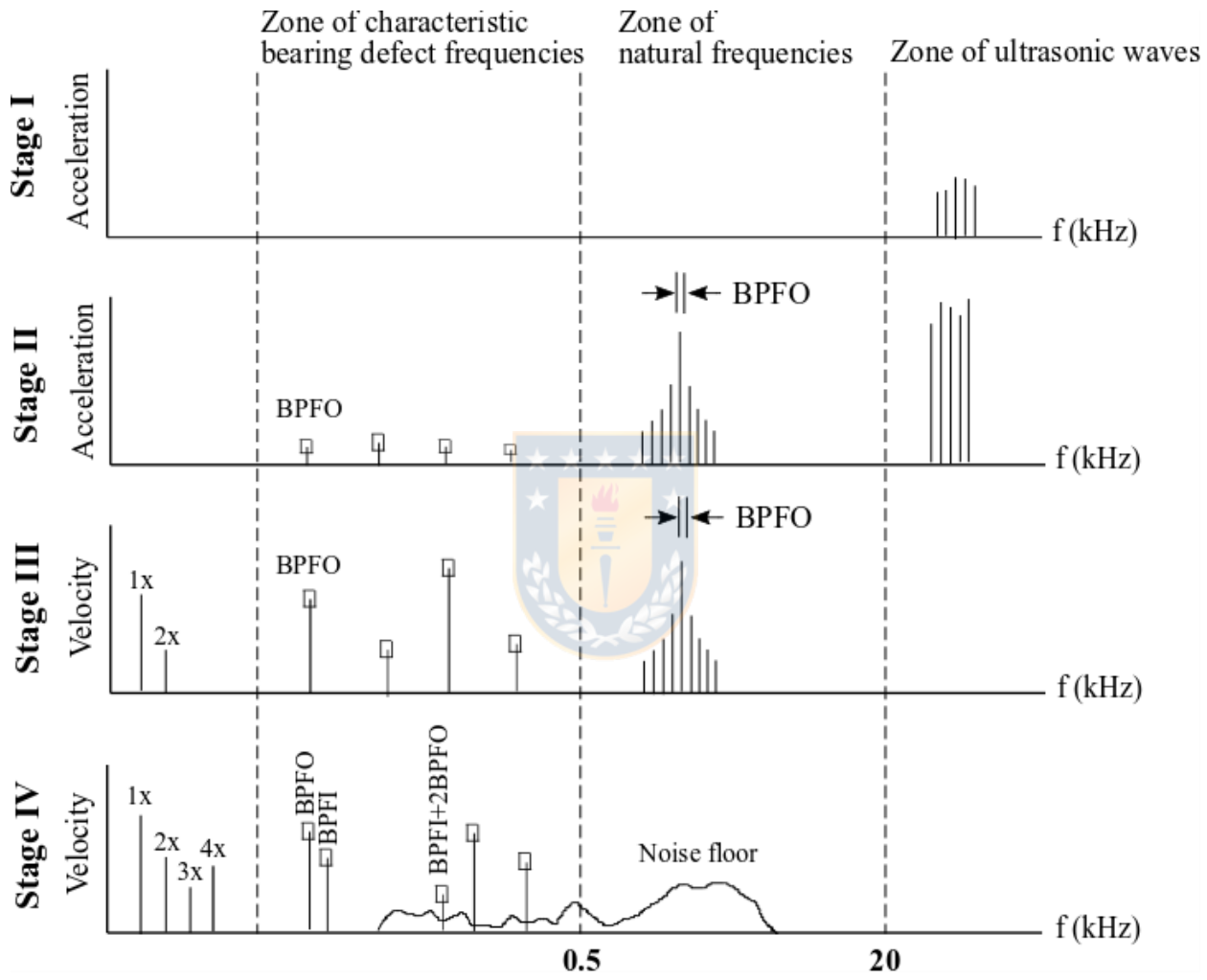

Figure 11. Stages of typical bearing fault development.

4.3 Acoustic emission

Acoustic emissions are transient elastic waves generated from a rapid release of strain energy caused by a deformation or damage within a material or on its surface [Mathews 1983]. In other words, under mechanical stresses, structural alteration occurs in a solid material, which results in quick delivery of strain energy which in turn generates transient elastic waves. In this investigation acoustic emissions are defined as the transient elastic waves generated by the impact-like interaction of two surfaces in relative motion. Analysis of AE is considered as one of the most suitable tools for bearing health monitoring

[Shiroishi 1997, Mba 2006]. Even many years ago acoustic emission measurements were already used on very slow-speed rotating machinery with promising results [Jamuludin 2001, Mba 1999].

The advantage of AE monitoring over vibration monitoring, as explained in section 4.2, is that the former can detect subsurface cracks, whereas the latter can detect defects only when they appear on the surface. Furthermore, due to the high-frequency content of the AE signatures typical mechanical noise (with frequency less than 20 kHz) is eliminated.

4.4 Vibration

Any rotating machinery produces a vibration signature that is strongly related to system performance and condition. Any potential fault will amplify vibration signal's energy or even distort the vibration waveform and spectrum.

That is the reason why for years the vibration analysis has been an established technique for detecting early stages of bearing defects [Mathew 1984, McFadden 1990]. When the defect in any component of the roller bearing comes in contact with the surface of another element an impact force is generated. This impact will cause an impulsive force in the bearing, which has a very short duration and causes a transient vibration.

But as mentioned in section 4.1 the energy generated from slow-speed bearings might not show an obvious change in signature and can become undetectable using conventional vibration measuring equipment and techniques. Hence the main challenge of vibration monitoring of slow-speed bearings are low defect frequency, high instrumentation noise and need of a long record and processing time for frequency analysis. Furthermore, as explained in section 4.2 the analysis of vibration signal signature from a defective bearing may not indicate the defect at the initial stage.

Despite the mentioned difficulties there are successful cases. For example, [Patel 2013] revealed that standard accelerometer can be used for vibration monitoring of slow-speed bearings.

4.5 Displacement vibration

Another approach used in some industrial applications focused on slow-speed bearing monitoring is the analysis of the shaft's relative displacement vibration. The displacement sensors are mounted in a position where they can register the relative radial distance between the sensor and the rotating shaft. The hypothesis is that when the balls pass over a defect a displacement vibration of the shaft according to the classic bearing failure pattern would be originated and that should be visible in the spectrum analysis. These measurements point to defects in stage III or IV.

.

CHAPTER 5

Experimental setup

5.1 Introduction

In this chapter important data regarding the experimental setup are presented. The data sheet of the RTM is shown, the characteristic defect frequencies (CDF) of the bearings are explained and the conditions of the measurements described.

5.2 Data sheet of the RTM

The data sheet of the RTM is presented in Figure 12.

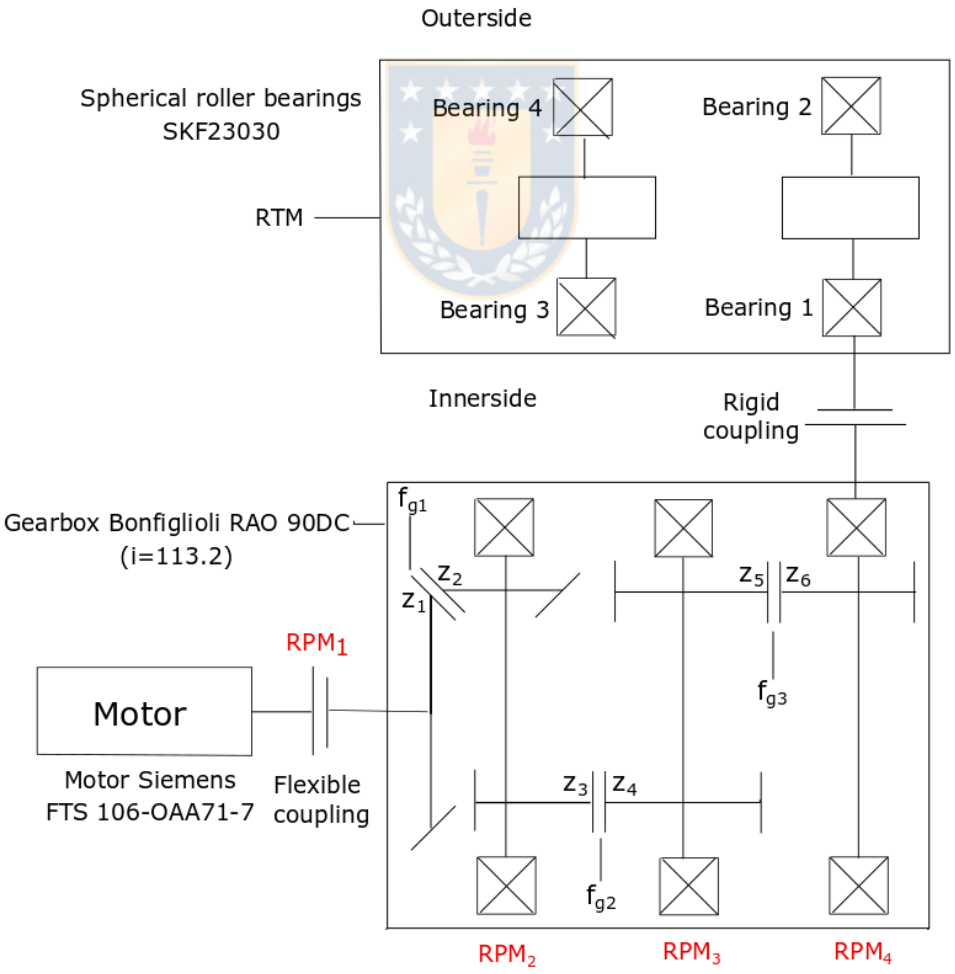

Figure 12. Data sheet of the RTM.

The number of teeth of each gear wheel in Figure 12 is shown in Table 5.

Table 5. Number of gear teeth.

Variable	Value
z_1	15
z_2	63
z_3	8
z_4	42
z_5	15
z_6	77

These values permit to calculate the RPMs indicated in Figure 12. The calculations are made considering RPM_4 as reference, whereby RPM_4 is estimated from the measured displacement signal as presented in chapter 7. Table 6 presents the values of the RPMs.

Table 6. Values of the RPMs of the RTM.

Variable	Value
RPM_4	Measured reference variable
RPM_3	$\frac{RPM_4 \cdot z_6}{z_5}$
RPM_2	$\frac{RPM_3 \cdot z_4}{z_3}$
RPM_1	$\frac{RPM_2 \cdot z_2}{z_1}$

The gear mesh frequencies indicated as f_g in Figure 12 depend on the number of gear teeth and the RPM. Table 7 shows the gear mesh frequencies of the RTM.

Table 7. Gear mesh frequencies of the RTM.

Variable	Value
f_{g1}	$z_6 \cdot RPM_4$
f_{g2}	$z_4 \cdot RPM_3$
f_{g3}	$z_2 \cdot RPM_2$

5.3 Characteristic defect frequencies of the bearing

Rolling element bearing fault recognition is based on the detection of some characteristic defect frequencies in the frequency spectrum. These frequencies depend on the bearing geometry, rotational speed and number of rolling elements. Therefore, they can be calculated theoretically.

Bearings basically consist of inner race, outer race, balls and cage as shown in Fig.13.

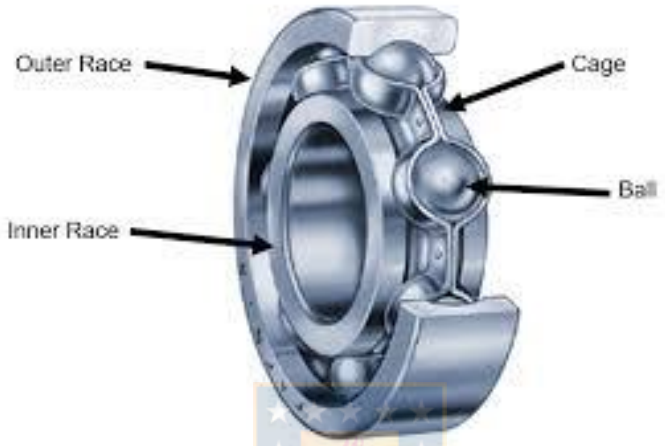

Fig. 13. Parts of a ball bearing (source: [www.hecoinc.com])

The characteristic defect frequencies are based on the different parts of the bearing and can be defined as follows [Saavedra 2005]:

a) Ball Pass Frequency Outer Race (BPFO) is defined as the fundamental frequency, which results when the ball passes over the defect such as a crack present in the outer race of the bearing.

b) Ball Pass Frequency Inner Race (BPFI) is produced when the ball passes over the defect present in the inner race of the bearing.

c) Ball Spin Frequency (BSF) is defined as the pulse repetition rate that occurs each time during the motion of the defective rolling element over other elements of the bearing.

d) Fundamental Train Frequency (FTF) is caused by a defect that occurs in the cage of the bearing.

For the spherical roller bearing SKF23030 CC/W33 the CDF are indicated in Table 8.

These CDF should not be visible at the vibration spectrum of a bearing working under normal working condition.

Table 8. CDF of spherical roller bearing SKF 23030.

Variable	Value
BPFI	$14.8 \cdot RPM_4$
BPFO	$12.2 \cdot RPM_4$
BSF	$5.09 \cdot RPM_4$
FTF	$0.45 \cdot RPM_4$

5.4 Conditions of the measurements

Four RTMs were selected for the measurements:

a) RTM 2 of the UT3: this RTM has been changed in Abril 2018, so it is considered as "healthy" and used as a reference of defect-free condition.

b) RTM 3 of the UT2, RTM 6 of the UT4 and RTM 8 of the UT4: these RTMs were selected because they never had been replaced since the UTs saw their first light.

The measurements were carried out during daytime between the 6th and 7th of July 2018.

Normally the fixed bearings suffer damage, which are the innerside bearings of the RTMs as shown in Figure 7. That are the bearings 1 and 3 in Figure 12. All the innerside bearings of the 4 RTMs were measured, that means 8 bearings in total. Additionally, in case of the older RTMs almost all outerside bearings were also included in the measurements, only a few could not be analyzed because of access difficulties on site.

For the AE, ACC and displacement vibration measurements four sensors were used:

a) Kistler wideband sensor, Model 8152B11 for the acoustic emission measurements. The frequency range of this sensor is 50 kHz to 400 kHz.

b) Two IMI vibration sensors, Model 603C01 for the acceleration measurements in horizontal and vertical direction. The sensitivity of this sensor is 100 mV/g and the frequency range 0.5 Hz to 10000 Hz.

c) Bently Nevada proximitor sensor, Model 20885-0 for the displacement measurements. The sensitivity is 200 mV/mils.

The sensors are shown in Figure 14 and the data sheets of the Kistler and the IMI sensor are presented in Appendix A.

Figure 15 shows the mounting of the sensors. The AE sensor was mounted directly to the bearing case using silicon grease as a coupling element, and fixed by means of adhesive tape. The accelerometers were mounted on the casing using magnetic mounting bases in horizontal (H) and vertical (V) direction. The displacement sensor was mounted with a magnetic base and a holding bracket as shown in Figure 15.

(a) (b) (c)

Figure 14. Measurement sensors. (a) Kistler wideband sensor. (b) IMI vibration sensor. (c) Bently Nevada proximitor sensor.

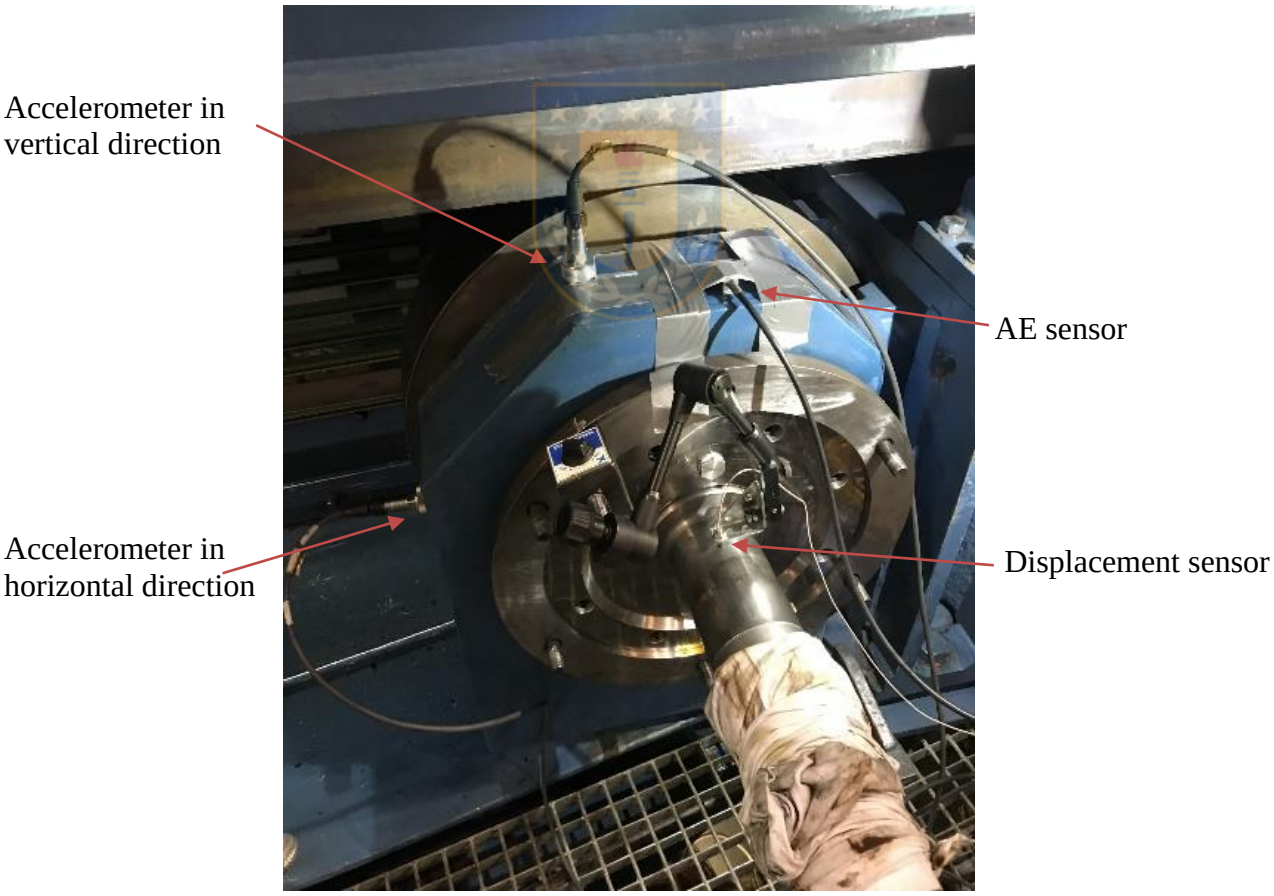

Figure 15. Sensor mounting.

Afterwards the enclosure was rotated clockwise with a speed between 1.3 °/s and 1.4 °/s for about 200 s in every measurement. All measurements were done simultaneously with a sampling frequency of 1 MHz for the AE, 51.2 kHz for acceleration vibrations and 5.12 kHz for displacement vibrations. Finally, all the measurement data were saved in the computer.

CHAPTER 6

Techniques used for signal processing

6.1 Introduction

Different methods are used for detection and diagnosis of slow-speed bearing defects. The techniques which were applied in this work are detailed in this chapter.

6.2 Time-domain approach

In the waveforms of the ACC and AE local bearing defects can be detected by observing the presence of periodic transients due to the impact of the rolling element with the defects. Especially in case of the AE the presence of bursts with a periodic pattern in the waveform is a sign of a bearing defect, because the bursts are generated by the interaction of the rotating elements with the faulty zone. In this case the bearing failure detection is based on the observation of differences between the AE generated by healthy and faulty bearings. The AE signal of a healthy bearing has a noise-like shape, whereas in case of a defect several repetitive bursts are observed.

6.3 Frequency-domain approach

Frequency-domain analysis is a traditional technique and is applied using the Fast Fourier Transform (FFT) algorithm as a computational efficient operation of the Discrete Fourier Transform (DFT) [Saavedra 2005]. Sometimes the characteristic defect frequencies can be identified in the acceleration spectrum [Tandon 1993]. The frequency-domain technique can provide information about the location of the bearing fault by analyzing the peaks in the spectrum at bearing characteristic defect frequencies. It has also been observed that, in case of a defect on a moving element such as the inner race, the spectrum has shaft rotational speed sidebands [Saavedra 2005]. The sidebands around the BPFI are present because as the inner race defect passes through the load zone it creates amplitude modulated vibration signal.

Especially in slow-speed bearings it is difficult to observe clear spectral components at the defect frequencies, because vibrations from outer sources often mask the vibration signal form the bearing unless the defect is sufficiently large. In order to improve the signal-to-noise ratio and make the spectral analysis more effective, the envelope detection can be used as explained in section 6.4.

6.4 Enveloping method

Envelope analysis, also known as high frequency resonance technique (HFRT) or demodulation, is considered as the benchmark method for bearing diagnostics at early steps, in particular for its high resolution capability [Azovtsev 1994]. Envelope analysis is based on the observation that bearing fault impulses are amplified by the resonance of the bearing housing or of the bearing itself thus improving the signal-to-noise ratio in the spectral analysis. Very high amplitude frequency components in a high frequency region are generated and CDF can be detected [McFadden 1984].

The process of the high-frequency resonance technique is that first the raw bearing signal is band-pass filtered in a high frequency region. Then there occurs signal enveloping, and finally the spectrum of the envelope signal is calculated using FFT algorithm [Randal 2011]. In this way the information is transferred to the low-frequency region.

The efficiency of the method for rolling element bearings depends strongly on the choice of the most impulsive band for demodulation. One possibility to determine the center frequency and bandwidth is observing high-energy frequency areas in the FFT spectrum [Howieson 2003]. Another approach to determine the most appropriate band for the envelope analysis is the spectral kurtosis, explained next.

6.5 Spectral kurtosis

The importance of spectral kurtosis (SK) in bearing fault diagnostics was highlighted by [Antoni 2006]. According to [Antoni 2006] the most important properties that makes SK very effective in bearing fault diagnosis can be summarized as follows:

a) SK is zero for a stationary Gaussian process.

b) SK is a constant function of frequency for a stationary process.

c) SK of a non-stationary signal (e.g. the vibration signal of a faulty rolling element bearing) in the presence of stationary noise has large values at frequencies where the signal-to-noise-ratio is high.

In order to get benefit from the properties of SK in the bearing defect diagnosis it is useful to have a representation tool that can visualize the center frequency and the bandwidth. [Antoni and Randall 2006] proposed as a representation tool a kurtogram. It is a representation of SK in a frequency and frequency resolution (Δf) plane. One year later an improvement was proposed by [Antoni 2007] who introduces some modifications named fast kurtogram.

As the SK is represented in the kurtogram, the optimal filter´s center frequency and bandwidth for the envelope analysis can be decided based on it and thus the performance of the conventional envelope analysis can be enhanced.

CHAPTER 7

Results and discussion

7.1 Introduction

After a thorough analysis of all condition monitoring measurements described in section 5.4 the interesting results were selected, and are presented as well as discussed in this chapter.

7.2 UT3-RTM 2, bearing 3, analysis period: 60 s to 80 s

As explained in section 5.4 the RTM 2 of the UT3 had been replaced in Abril 2018. So it can be considered as “healthy” and used for result comparison with the other three measured RTMs which have never been changed.

Although both innerside bearings of the RTM 2 were checked, in this section the results obtained from the innerside idle bearing (bearing 3 according to Figure 12) during the measurement period of 60 s to 80 s are shown as a representative example.

As mentioned in section 5.3 the bearing fault recognition is based on the detection of characteristic defect frequencies (CDF) which are determined from the bearing defect factors and the rotational speed of the shaft (Table 8). The defect factors are obtained from open bearing databases. The speed is determined from the runout present in the displacement vibration (Figure 17). The obtained value of the RPM is 0.1905 Hz. The resulting CDF can be observed in Table 9. This table shows that the defect frequencies lie in the low-frequency range. In practice, these frequencies may be slightly different form the calculated values as a consequence of slippage of balls which usually occurs due to the uneven load distribution on the bearing. Generally, the difference fluctuates between 1% and 3% [Saavedra 2005]. One common feature of the bearing´s CDF is that they are not integer multiples of the rotational speed of the shaft [Saavedra 2005].

Figure 16 shows the waveform of all measured variables. The AE waveform has a noise-like shape and no periodic succession of bursts can be observed. Also in case of the ACC the waveform shows in the horizontal (H) as well as in the vertical (V) direction only noise, no transients with a periodic pattern can be observed. The displacement signal shows no transients as well, only the measurement of the shaft runout. In Figure 17 apart the displacement spectrum mentioned before the envelope spectrum of the AE signal without filter together with the velocity spectra of the accelerometers in horizontal and vertical direction are shown. The same results obtained from the waveforms are valid also for the spectra. In case of the AE and the velocity spectra no periodic pattern of peaks can be recognized, and the spectrum of the displacement shows as mentioned before only the RPM of the wheel shaft. So no CDF were observed. In this case no further analysis is necessary.

In summary, the measurement results of the RTM 2 in the UT3 reveal that the RTM is in good condition, the bearings do not show any signs of defect.

Table 9. Characteristic defect frequencies. Speed: RPM_4 = 0.19 Hz.

Variable	Frequency [Hz]	Period [s]
RPM_4	0.19	5.3
BPFI	2.82	0.36
BPFO	2.32	0.43
BSF	0.97	1.03
FTF	0.09	11.1

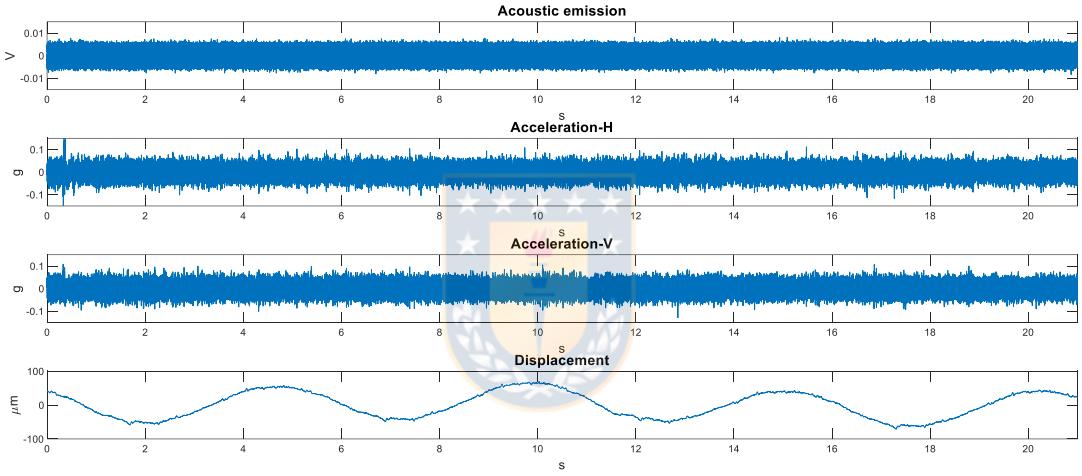

Figure 16. Waveforms, UT3-RTM 2-bearing 3.

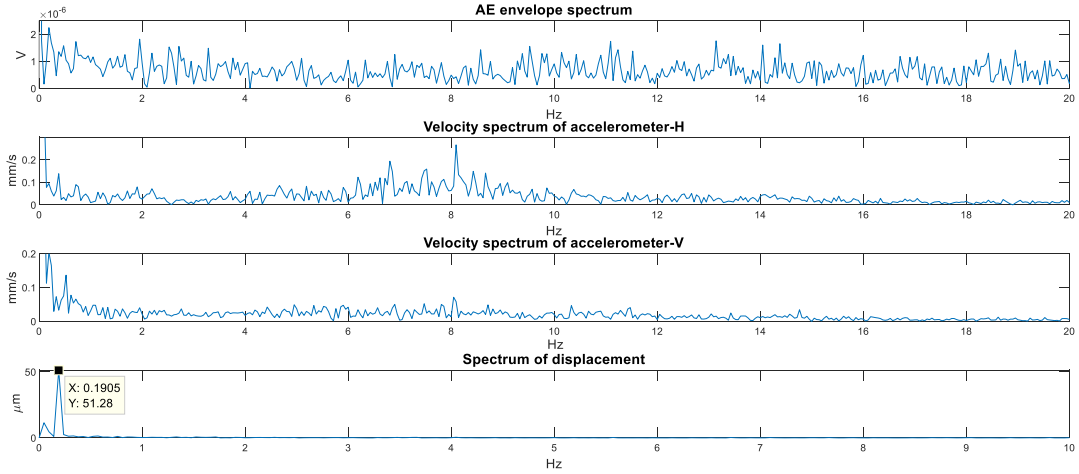

Figure 17. Spectrum analysis without filter, UT3-RTM 2-bearing 3.

7.3 UT2-RTM 3, bearing 2

The RTM 3 of the UT2 belongs to the group of measured RTMs which have never been replaced. Below the results of two different measurement periods of the outerside motor driven bearing (bearing 2 according to Figure 12) are shown as representative examples for this bearing.

7.3.1 First analysis period: 92 s to 110 s

The RPM of the wheel shaft are obtained from the displacement spectrum shown in Figure 19 as explained in section 7.2. In this case the value of the RPM is 0.2105 Hz and the corresponding CDF are shown in Table 10.

Table 10. Characteristic defect frequencies. Speed: RPM_4 = 0.21 Hz.

Variable	Frequency [Hz]	Period [s]
RPM_4	0.21	4.75
BPFI	3.12	0.32
BPFO	2.57	0.39
BSF	1.07	0.94
FTF	0.09	11.1

Figure 18 shows the time waveform of all measured variables. In the AE waveform, a periodic succession of bursts can be observed, separated by 0.43 s. This period is associated with the BPFO as indicated in Table 10 considering the possibility of a slightly difference between the theoretical and measured value as explained in section 7.2. The difference between the two values in this case is 8.9%, that means outside the range of 1% to 3% considered by [Saavedra 2005]. The determination of the BPFO depends on the frequency resolution, which in this case is $1/19\ s\ =\ 0.053\ Hz$. That means that in case of the analysis period of 19 s the 1X component only can have integer multiples of 0.053 Hz. If the real RPM are in the range of $0.2105\ \pm\ 0.053/2$, the shown 1X component has always the value of 0.2105 Hz. That is why the possibility of a difference between the theoretical and measured value of the BPFO higher than 3% exists. The waveform of the accelerations shows some small transients, but without any periodic pattern which could be associated with the CDF. In the waveform of the displacement measurement only the shaft runout can be observed.

Figure 19 shows the envelope spectrum of the AE signal without filter together with the spectrum of the velocity calculated from the acceleration vibration, and the spectrum of the displacement. As expected, also in the envelope spectrum of the AE a set of harmonic components can be observed and the corresponding frequencies are obtained directly. The fundamental frequency indicated in the figure is 2.263 Hz, a value which match relatively closely with the theoretical BPFO value of 2.57 Hz as indicated in Table 10. The difference is 11.9% which probably has the same reason as explained before. As the envelope signal is highly periodic, several harmonics of the BPFO are also clearly observed. On the other

hand, the velocity spectra have a noise-like shape. The fact that the symptoms of the bearing fault are so clearly visible in the high frequency range, but not observable in the low frequencies is related to an incipient defect as explained in section 4.2. An incipient defect should also not be recognizable in the displacement spectrum as can be observed in Figure 19.

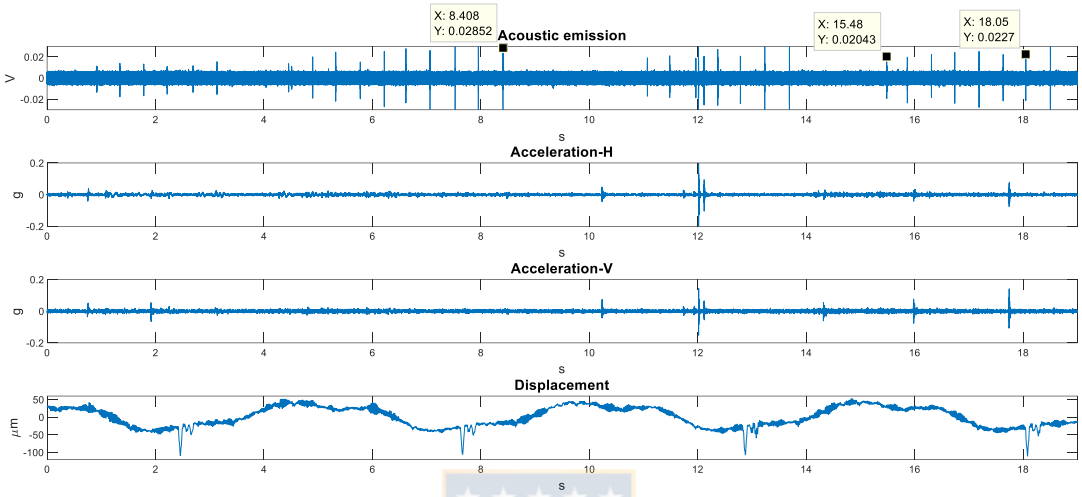

Figure 18. Waveforms, UT2-RTM 3-bearing 2, analysis period: 92 s to 110 s.

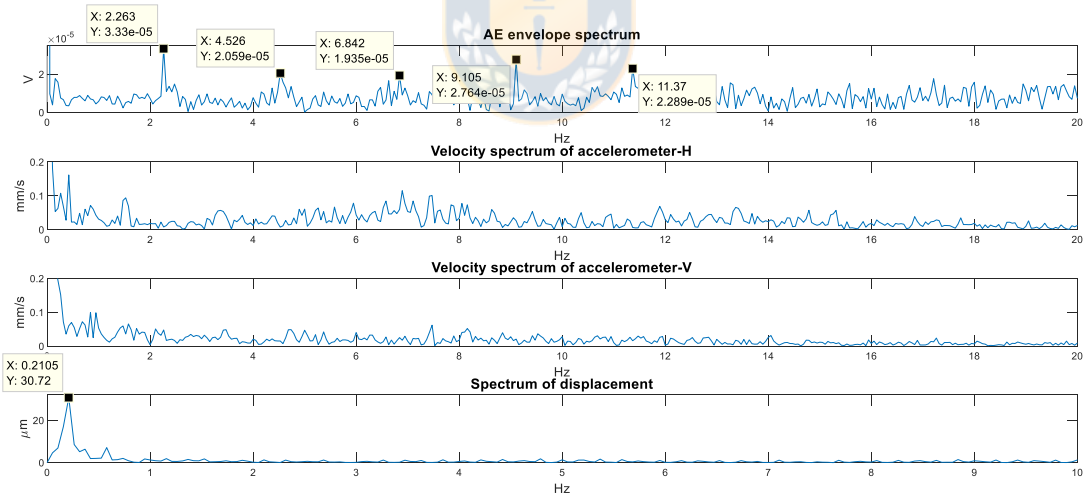

Figure 19. Spectrum analysis without filter, UT2-RTM 3-bearing 2, analysis period: 92 s to 110 s.

The high frequency FFT spectrum of the AE is shown in Figure 20. This spectrum helps to choose a filter before applying the AE envelope spectrum by observing high frequency energy areas. As marked in the figure a filter around 98 kHz is used. The fast kurtogram was also used as an alternative to select the most suitable frequency band for demodulation. Fig. 21 shows the kurtogram where is seen that the Kurtosis (i.e. the impulsiveness feature of the signal) is maximum in the band from 21.972 kHz to 22.460 kHz. The decomposition level 10 means that the signal is progressively decomposed via a filter bank

structure in $2^{10} = 1024$ frequency bands and the SK is calculated at each band. The color bar shows the range of SK values. As the indicated center frequency of 22216 Hz is outside of the AE sensor frequency range mentioned in section 5.4, the AE spectrum is only filtered around 98 kHz. Figure 22 shows the resulting envelope of the AE, whereas the filtered envelope spectrum can be observed in Figure 23. The same results shown in Figure 18 and 19 are obtained, the filter in this case only enhance the characteristic bursts.

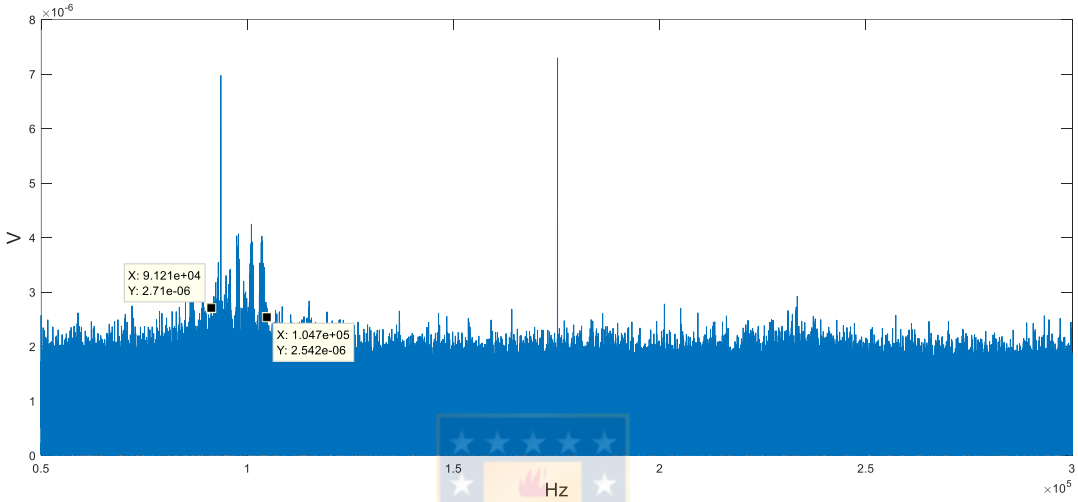

Figure 20. FFT spectrum of AE, UT2-RTM 3-bearing 2, analysis period: 92 s to 110 s.

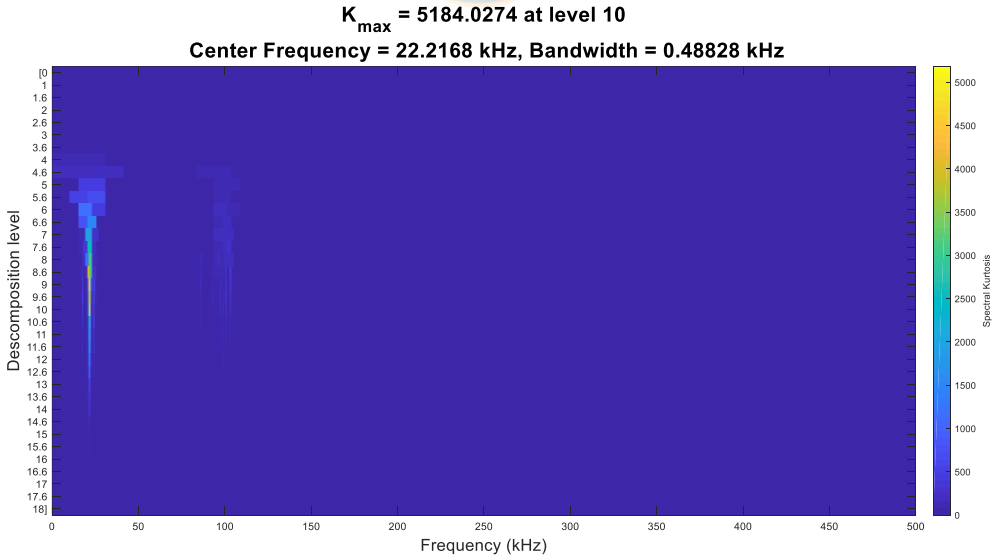

Figure 21. Kurtogram of AE.

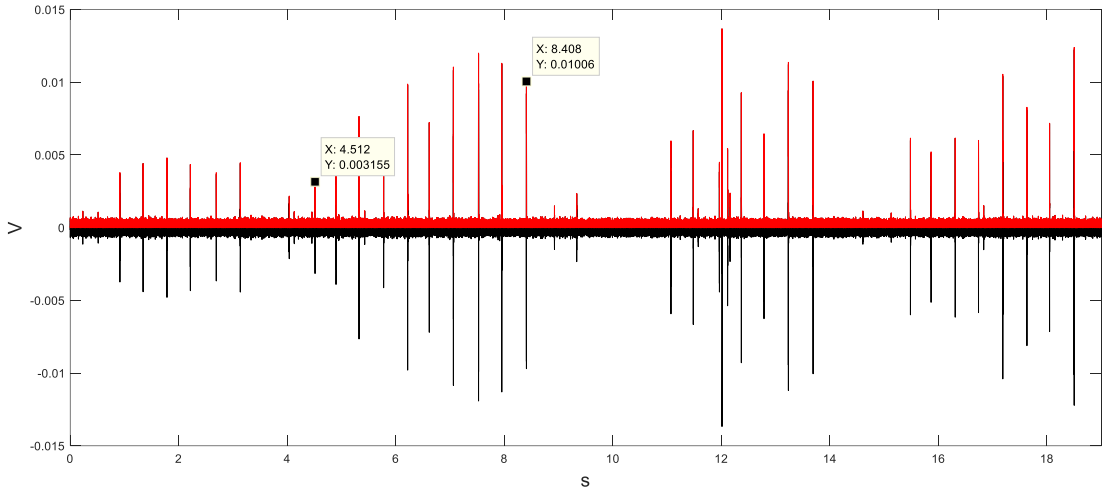

Figure 22. Envelope of filtered AE (center frequency: 98 kHz).

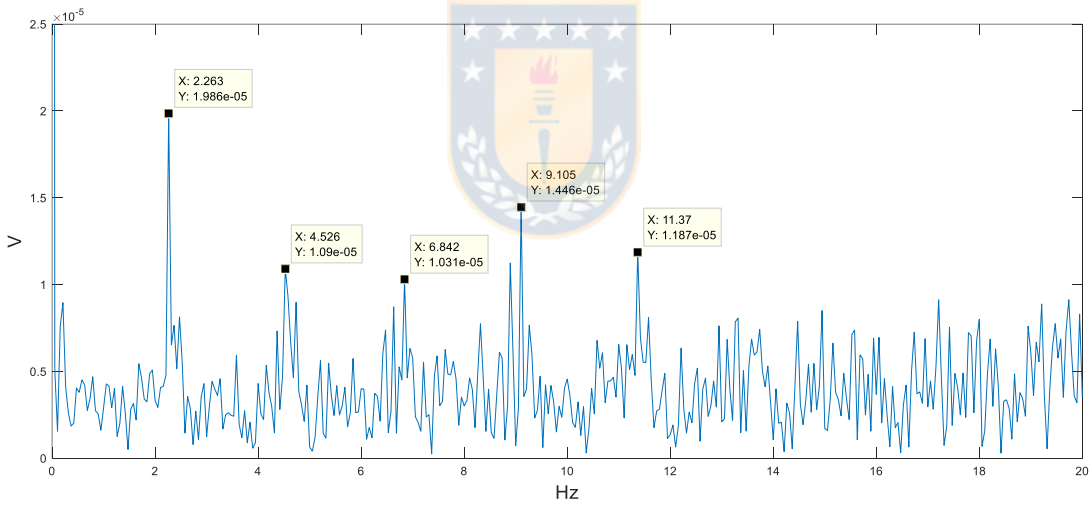

Figure 23. Filtered envelope spectrum of AE (center frequency: 98 kHz).

Next the acceleration high frequency spectrum has to be analyzed because of the possibility that the bearing defect is in stage II. The ACC-H and ACC-V spectra can be observed in Figure 24. As detailed in section 6.3 especially in slow-speed bearings it is difficult to observe clear spectral components at the defect frequencies. Therefore, the envelope detection is used as explained in section 6.4 to improve the signal-to-noise ratio and make the spectral analysis more effective. As the efficiency of this method depends strongly on the choice of the most impulsive band for demodulation, the zones of resonance frequencies in the acceleration spectra obtained applying the FFT are filtered. Center frequency and bandwidth are determined by observing high-energy frequency areas in the acceleration spectrum.

Figure 24 shows filter examples of the high frequency acceleration spectrum. In this case the ACC-H spectrum is filtered between 4229 Hz and 5613 Hz, whereas the filter range of the ACC-V spectrum is 4215 Hz to 5370 Hz. More filter ranges were used, but did not reveal different results.

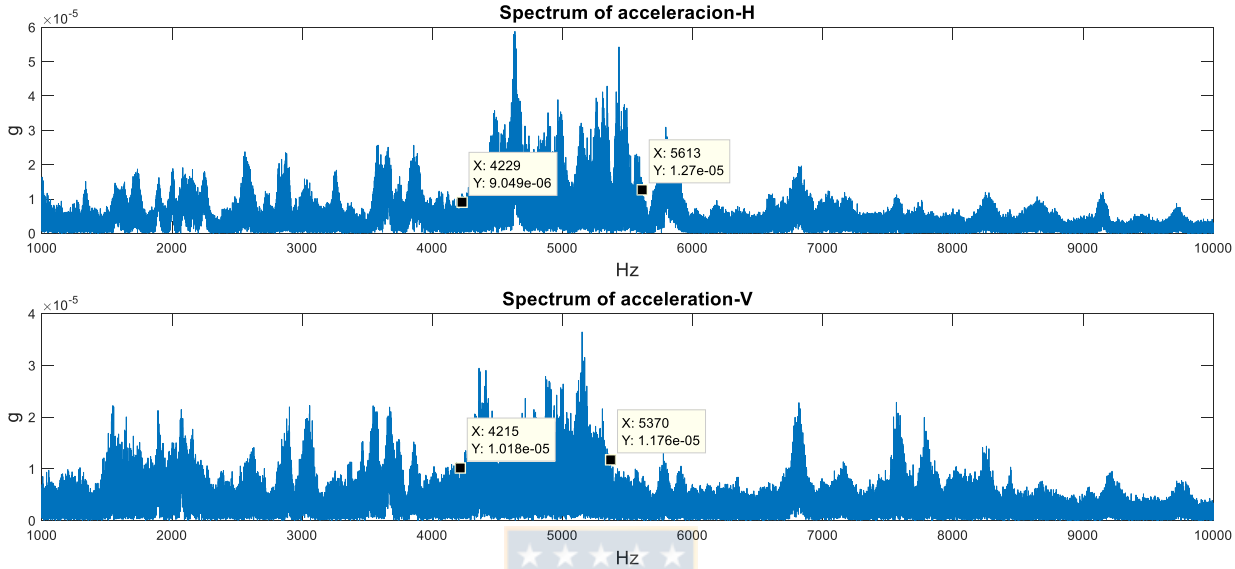

Figure 24. Acceleration high frequency spectra with marked filter ranges.

The result of the filtered envelope spectrum of ACC-H is shown in Figure 25, whereas the result of ACC-V can be observed in Figure 26. Both figures show that the resulting envelope spectra have a noise-like shape, where no clear components associated to the CDF can be found. These results lead to the conclusion that the acceleration vibration measurement is not suitable for detection of an incipient bearing defect in the RTM. Generally high frequency energy is severely affected by the distance of the point where the accelerometer is mounted (signal transmission path), existing the possibility to complicate the transmission on high frequency components. This is due to the fact that high frequencies are attenuated by the distance from the source of vibration to the accelerometer mounting position thus causing the high frequency information to get masked by other vibration sources.

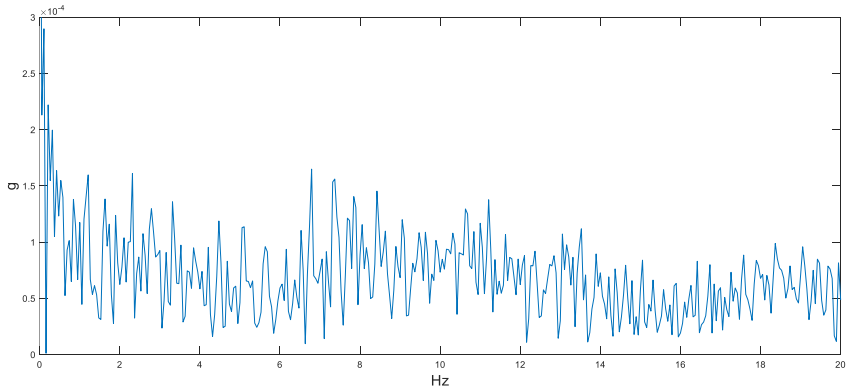

Figure 25. Filtered ACC-H envelope spectrum (center frequency: 4921 Hz).

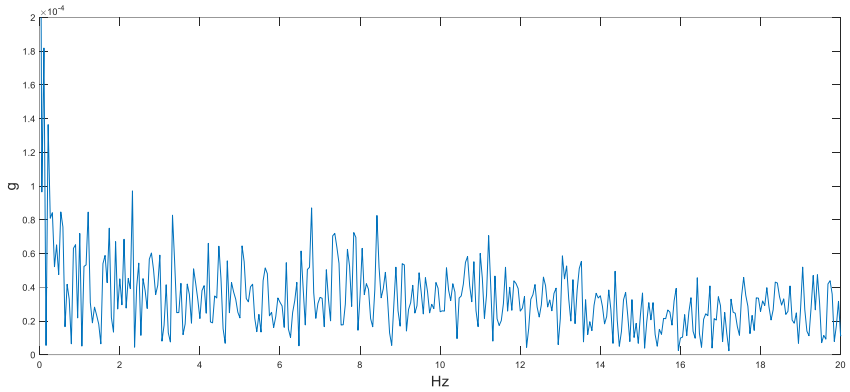

Figure 26. Filtered ACC-V envelope spectrum (center frequency: 4793 Hz).

The displacement vibration analysis was performed under the assumption that a fixed sensor is used. But in reality this not holds fully because the sensor is mounted by a support system consisting of a holding bracket. To take this into account also the natural frequency of the mounting system is measured by an impact test as can be observed in Figure 27. Although the natural frequency of the holding arm does not coincide with the CDF, it is important to distinguish if the shaft is moving or the natural frequency of the holding arm is excited. Additionally, the energy level increases when the natural frequency of the support system is excited. Furthermore, the bearing defect could also move the holding arm each time an impact with sufficient energy is generated because the ball passes over the defect. Therefore, the displacement spectrum was filtered around the natural frequency of 42.65 Hz as indicated in Figure 27. The filtered envelope spectrum is shown in Figure 28 where no CDF can be observed.

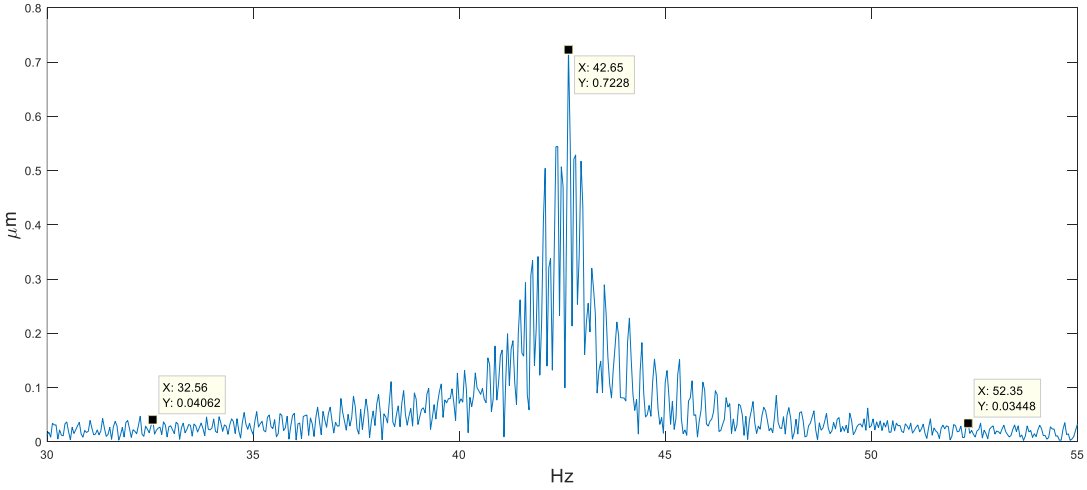

Figure 27. Natural frequency of the displacement sensor´s support system.

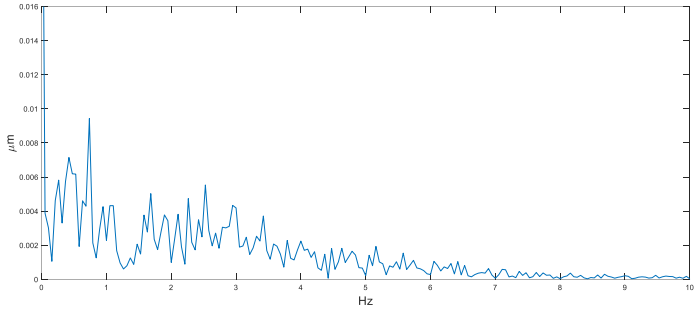

Figure 28. Filtered envelope spectrum of displacement (center frequency: 42.65 Hz).

In summary, the acoustic emissions of the bearing 2 of the RTM 3 (UT2) show signs of an incipient defect in the outer race, which acceleration vibration and displacement vibration do not reveal. Probably it is an incipient bearing failure (stage I) where the defect can be identified only by techniques that work efficiently at high frequency regions, how it does the AE analysis. Lubricant analysis is recommended, as well as periodic monitoring of the bearing defect.

7.3.2 Second analysis period: 120 s to 130 s

The results obtained in section 7.3.1 are valid for the most part of the totally 279 seconds measured of the bearing 2 of the RTM 3. But between the sections which show the characteristic bursts clearly in the waveform and the unfiltered AE envelope spectrum, there are some sections where these bursts are not visible. One example is the period between 120 s to 130 s. No bursts can be observed in the waveforms as shown in Figure 29, neither in the different spectra in Figure 30. The RPM obtained from the displacement spectrum has a value of 0.1818 Hz. That means that the rotational speed of the RTM wheel shaft changed with regard to the first analysis period. This is expectable in slow-speed machines. The resulting CDF are shown in Table 11.

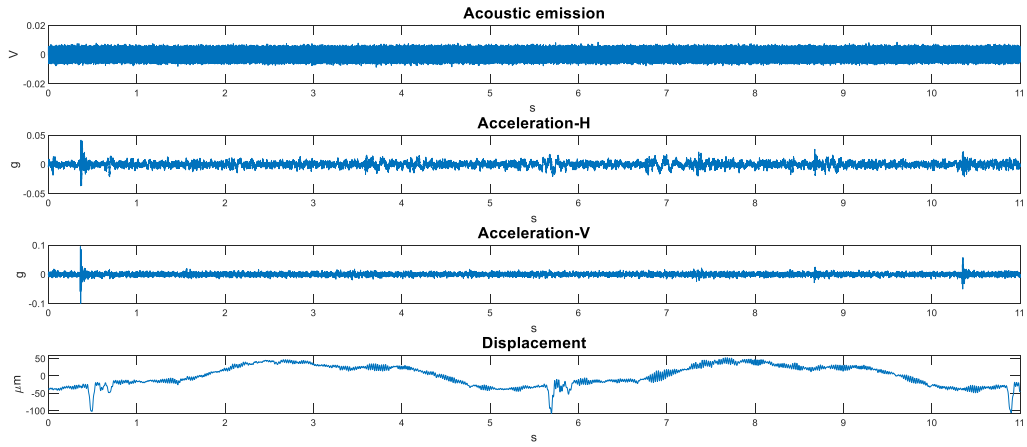

Figure 29. Waveforms, UT2-RTM 3-bearing 2, analysis period: 120 s to 130 s.

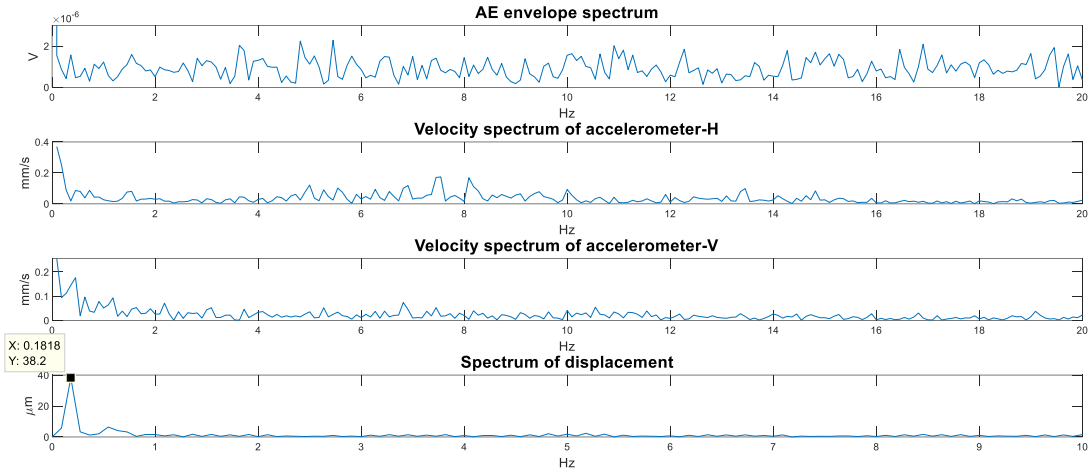

Figure 30. Spectrum analysis without filter, UT2-RTM 3-bearing 2, analysis period: 120 s to 130 s.

Table 11. Characteristic defect frequencies. Speed: RPM_4 = 0.18 Hz.

Variable	Frequency [Hz]	Period [s]
RPM_4	0.18	5.5
BPFI	2.69	0.37
BPFO	2.22	0.45
BSF	0.93	1.08
FTF	0.08	12.5

According to the results obtained above, also the high frequency FFT spectrum of the AE does not show a high frequency energy area which could be filtered. This can be observed in Figure 31. Having in mind that exists the possibility that the frequency information got masked because of a lower energy level, the AE spectrum is filtered using the same center frequency as in section 7.3.1, it means 98 kHz. The resulting filtered envelope spectrum is shown in Figure 32. No peaks associated to the CDF can be observed. The marked peaks correspond to integer multiples of the rotational speed of the shaft.

In summary, there are sections of the measurement where the bearing defect is not detectable probably due to the incipient defect. Therefore, a sufficient record time during the measurement is very important.

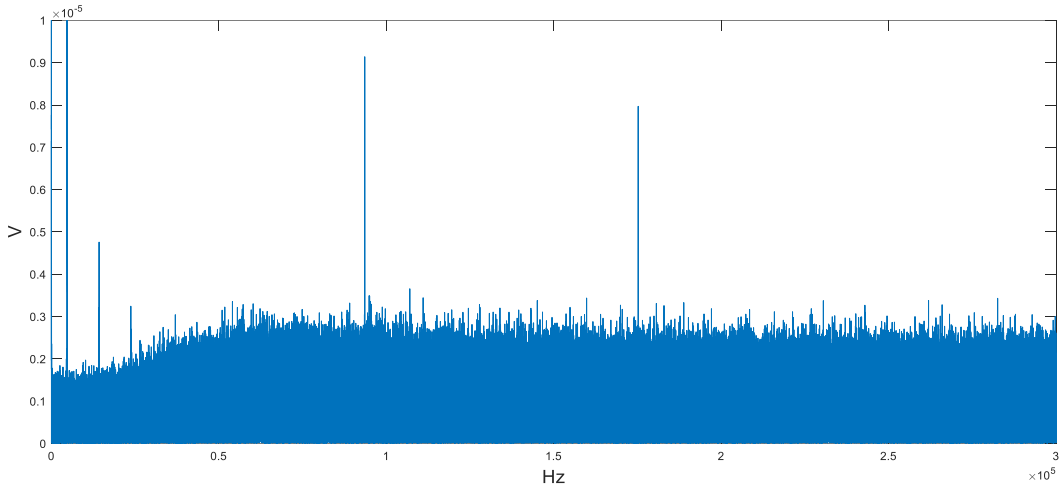

Figure 31. FFT spectrum of AE, UT2-RTM 3-bearing 2, analysis period: 120 s to 130 s.

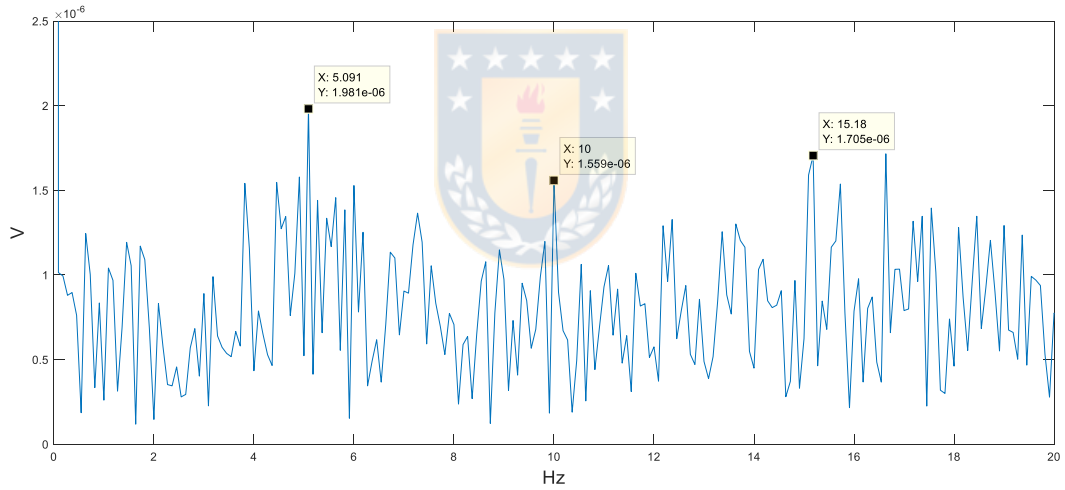

Figure 32. Filtered envelope spectrum of AE (center frequency: 98 kHz).

7.4 UT2-RTM 3, bearing 1, analysis period: 40 s to 61 s

In this section the analysis of the innerside motor driven bearing (bearing 1 according to Figure 12) measurement is presented. The RTM is the same as the analyzed in section 7.3, and again a representative section is selected, in this case the period form 40 s to 61 s.

The RPM of the wheel shaft obtained from the displacement spectrum shown in Figure 34 is 0.1818 Hz. The resulting CDF are shown in Table 11.

The analysis of this bearing is performed in the same way as explained in section 7.3.1. Figure 33 shows the waveform of all measured variables and Figure 34 the different spectra without filter.

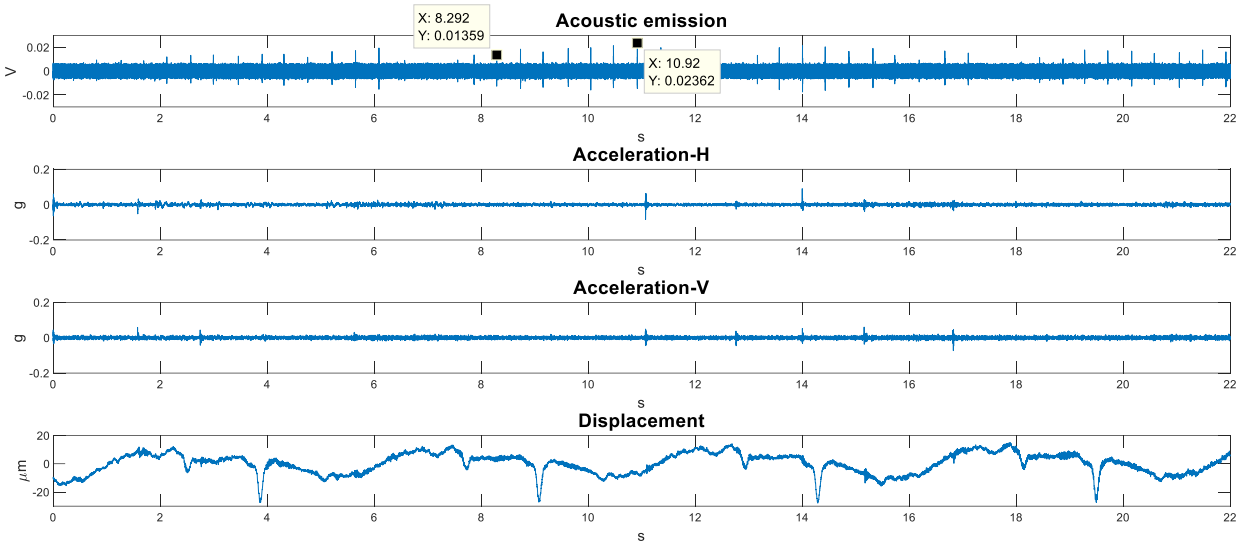

Figure 33. Waveforms, UT2-RTM 3-bearing 1.

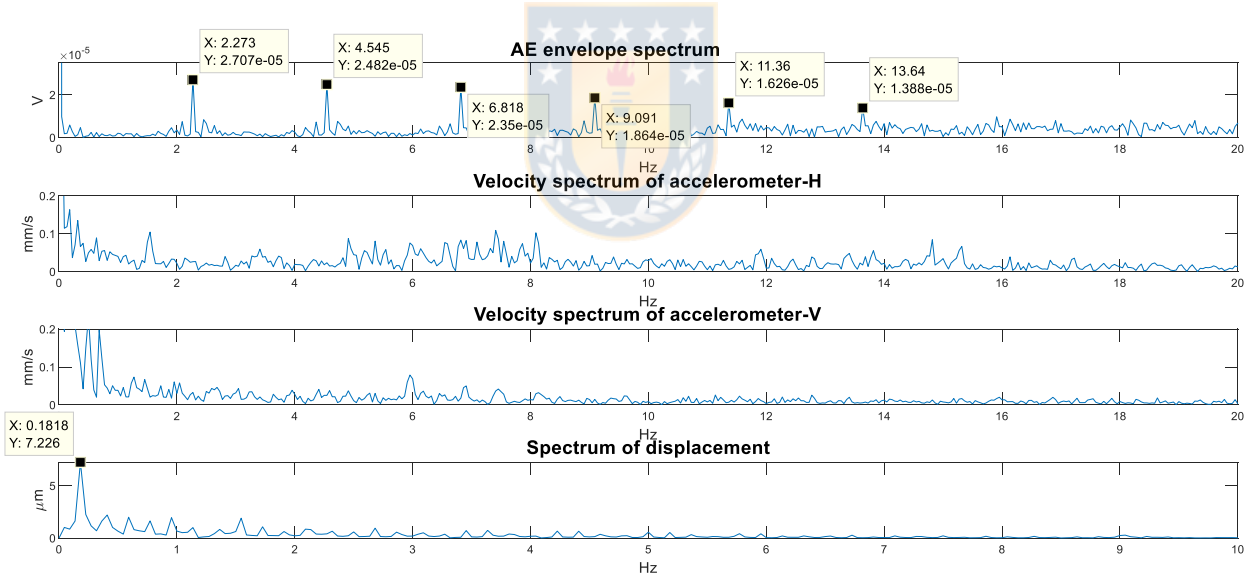

Figure 34. Spectrum analysis without filter, UT2-RTM 3-bearing 1.

A periodic succession of bursts separated by 0.44 s can be observed in the AE waveform. This period is associated with the BPFO as indicated in Table 12 considering again the possibility of a slightly difference between the calculated and measured value as explained in section 7.2. The difference between the two values in this case is 2.3%, which is within the expected range. Comparing the amplitude of the bursts with those shown in Figure 18, it can be observed that the amplitudes in this case are considerably

lower. In the waveform of the accelerations some small transients can be observed, but without any periodic pattern. In the waveform of the displacement measurement again only the shaft runout is shown.

As expected, in the AE envelope spectrum presented in Figure 34 a periodic pattern of several burst can be observed. The fundamental frequency is 2.273 Hz, a value which match closely with the theoretical BPFO value of 2.22 Hz. The difference is 2.4% which is acceptable as explained above. The velocity spectra of the accelerometers have a noise-like shape. As in section 7.3.1 also the acceleration high frequency spectra are analyzed, filters are selected and filtered envelope spectra of ACC-H and ACC-V are obtained. All spectra have only a noise-like shape. The corresponding figures of one example are shown in Appendix B.

The question now is if bearing 1 and bearing 2 present an incipient outer race defect, or the AE bursts of one bearing are transmitted to the other one. Thinking in the theory that the damage of the bearings is caused by high axial thrusts, a failure of the fixed bearings, that means of the innerside bearings (bearing 1 or 3) is more probable. The reported examples of RTM bearing damage described in section 1.1. have in certain way also confirmed this theory. However, comparing Figure 18 with Figure 33 the amplitudes of the bursts in the AE waveform are considerably higher in the bearing 2 (outerside). As the amplitude of the AE bursts is associated directly to the damage magnitude, it is more probably that in this case the bearing 2 presents an incipient outer race defect, and the bursts are transmitted to the bearing 1. But the other possibilities cannot be excluded. Therefore, as mentioned in section 7.3.1, lubricant analysis is recommended, as well as periodic monitoring of these bearings.

7.5 UT4-RTM 8, bearing 2, analysis period: 65 s to 73 s

The RTM 8 of the UT4 belongs also to the group of measured RTMs which have never been replaced. In this section the analysis of the measurement period 65 s to 73 s of the outerside motor driven bearing (bearing 2 according to Figure 12) is presented.

In this case the RPM of the wheel shaft cannot be obtained because the displacement sensor could not be installed due to access problems on site. But the waveform of the AE presented in Figure 35 shows some periodic bursts separated by 0.35 s, and in Figure 36 a periodic pattern of transients in the AE envelope spectrum can be observed. The fundamental frequency is 2.778 Hz. The high frequency FFT spectrum of the AE is shown in Figure 37. As explained in section 7.3.1, in this spectrum high frequency energy areas can be selected. A filter around 88780 Hz is applied. Figure 38 shows the resulting envelope of the AE signal and Figure 39 the filtered envelope spectrum. In Figure 38 bursts can be observed which are not visible in Figure 36. This is a clear example for the high resolution capability of the enveloping method improving the signal-to-noise ratio in the spectral analysis. Figure 39 presents the same result as Figure 37.

It is difficult to decide if the fundamental frequency of the periodic pattern of the observed peaks match with the BPFO or BPFI since the rotational speed of the shaft is unknown. But considering the low amplitude of the bursts it is probable that these bursts are generated by parametric vibrations. Parametric vibrations in bearings mostly are produced by a variation of its stiffness while the bearing is rotating and a constant force is acting, in this case the load due to the dome weight. That means that this vibration is generated due to different deformations of the bearing races and the rolling elements according to the position of the rolling elements with regard to the load. Figure 40 represents this effect graphically.

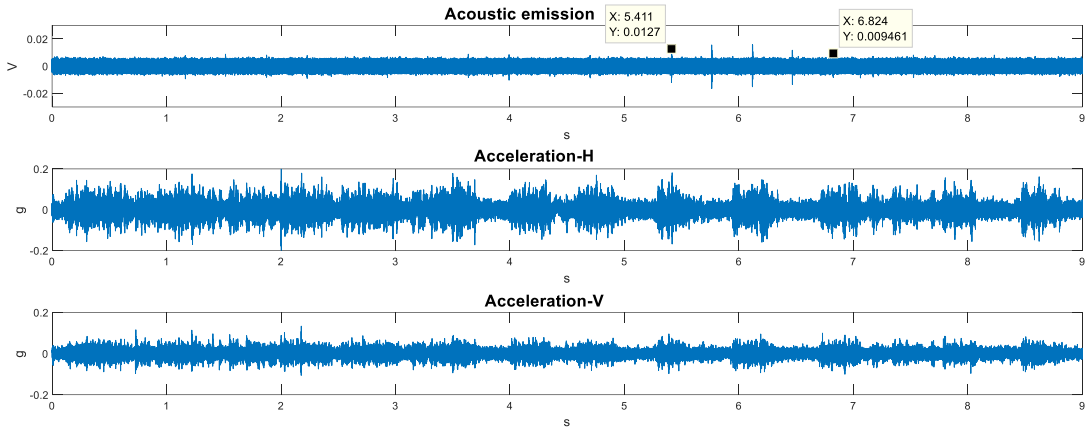

Figure 35. Waveforms, UT4-RTM 8-bearing 2.

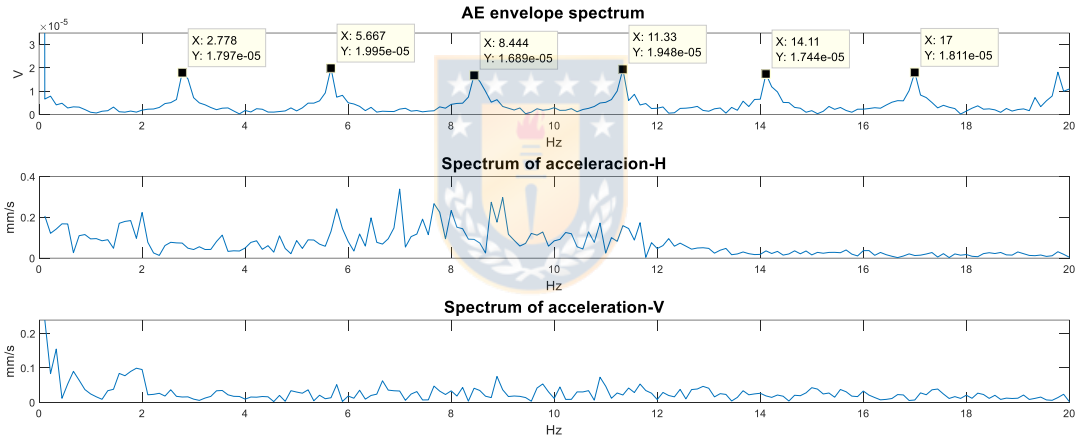

Figure 36. Spectrum analysis without filter, UT4-RTM 8-bearing 2.

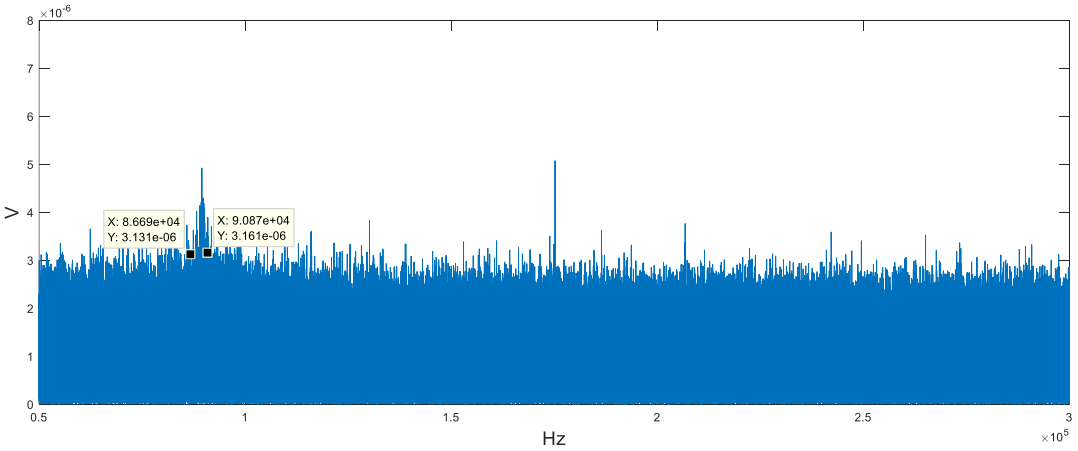

Figure 37. FFT spectrum of AE, UT4-RTM 8-bearing 2.

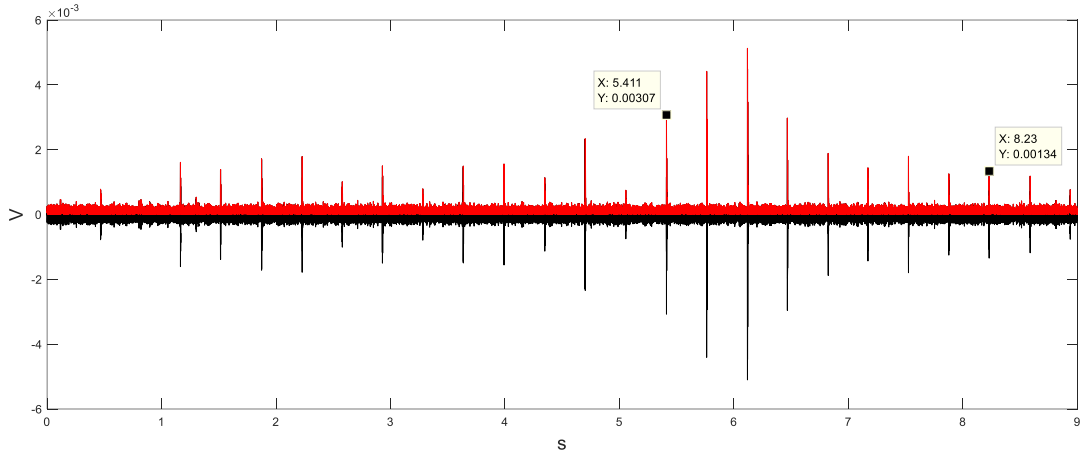

Figure 38. Envelope of filtered AE signal (center frequency: 88780 Hz).

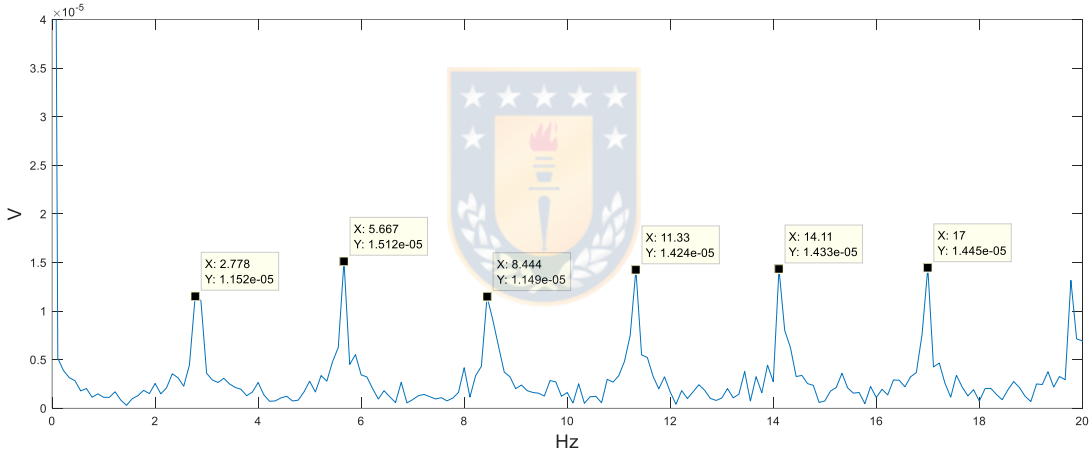

Figure 39. Filtered envelope spectrum of AE (center frequency: 88780 Hz).

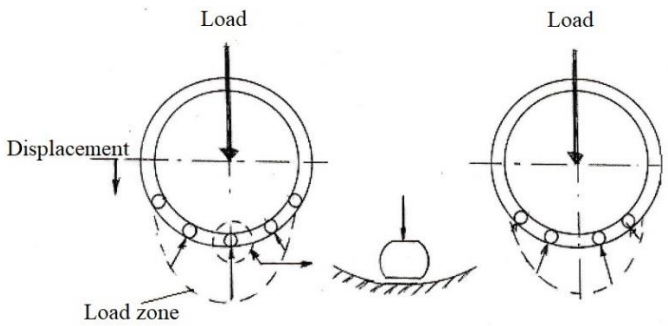

Figure 40. Generation of parametric vibrations (source: [Saavedra 2005]).

CHAPTER 8

Conclusions and perspectives

8.1 Conclusions

In this research work, the load distribution of the dome weight on the RTMs in UT1 and UT4 was analyzed inspired by the hypothesis that the damage of the bearing of the RTMs is caused by an unequal load distribution. A method to estimate the dome weight distribution was developed. The method consists in using Fujifilm´s Prescale measurement films which permit the obtainment of images of the contact pressure and its distribution between the vertical wheel and the rail. The results revealed that in both UTs some RTMs present an important underload up to 32% less than considered by design. Contrary, neighboring RTMs compensate this situation by supporting an overload up to 43% higher compared to the nominal load. The results lead to the conclusion that unequal load distribution of the dome weight on the RTMs exists. Since the maximum permissible axial load of the bearings of the RTMs is even below the minimum axial force which is released when the wheel of a RTM with normal load suddenly slips, it can be concluded that the stick-slip effect already per se contributes to excessive axial thrust, which can damage the bearings of the RTMs. Therefore, any bogie misalignment and even more any overload on the RTMs has to be avoided.

From the fact that it is difficult to avoid any bogie misalignment results the need to develop a condition monitoring method. This was done in the second part of this research work. The RTM wheel shaft has a very slow rotational speed which makes it difficult to monitor the bearings because of the generation of low impact energy due to the relative motion of the components when defects are present. Four RTMs were selected for the measurements. One which had been replaced three months before, and three which have never been changed since telescope´s first light. The recently replaced RTM was selected as a reference of defect-free condition. The inner- and outerside bearings were analyzed. AE, acceleration vibration and displacement vibration of the shaft were measured and the signals processed using time- and frequency-domain based techniques such as enveloping method and spectral kurtosis. One incipient bearing failure of the outer race of the RTM could be identified by the acoustic emissions, whereas acceleration and displacement vibration did not provide any signs of defect. These results lead to the conclusion that the AE analysis can detect incipient defects even in slow-speed bearings, whereas acceleration and shaft displacement vibration measurements are not as suitable for the detection of early stage bearing failure in the RTMs.

8.2 Perspectives for future work

Based on the obtained results, the load distribution of the dome weight on the RTMs should be analyzed also in UT2 and UT3. Then the RTMs with overload should be selected and their condition be checked at least by acoustic emission measurements.

In case of identifying an incipient defect, lubricant analysis is recommended, as well as periodic monitoring of the bearing defect.

In addition, the development of a technology for implementing a periodic condition monitoring on side is suggested. This would permit the monitoring of the evolution of a bearing defect, thus allowing to plan the RTM maintenance and to avoid unexpected and/or catastrophic failures.

Moreover, based on the results of the maximum permissible axial load the selection of the fixed RTM bearings should be re-evaluated.

REFERENCES

Antoni J.
The Spectral Kurtosis: a useful tool for characterizing non-stationary signals.
Mech. Syst. Sign. Process 20 (2) (2006) 282-307.

Antoni J.
Fast computation of the kurtogram for the detection of transient faults.
Mech. Syst. Sign. Process 21 (1) (2007) 108-124.

Antoni J., Randall RB.
The Spectral Kurtosis: Application to the Vibratory Surveillance and Diagnostics of Rotating Machines.
Mech. Syst. Sign. Process 20 (2) (2006) 308-331.

Azovtsev YA., Barkov AV., Yudin LA.
Automatic diagnostics and condition prediction of rolling element bearings using enveloping methods.
Vibration Institute Proceedings, 18th Annual Meeting, Hershey, Pennsylvania (1994).

Bigelow B., Loewen N., van Vuuren E., Burgett W.
A survey of enclosure suspension and rotation system for 3-15m telescopes.
Proc. SPIE 9906, Ground-based and Airborne Telescopes VI, 99060E (2016).

Bugueno E.
Elaboración de un plan de mantenimiento para los mecanismos de rotación de los domos de los telescopios del observatorio europeo austral, VLT Cerro Paranal.
Diploma Thesis, Department of Civil Industrial Engineering, Universidad Arturo Prat, Antofagasta (2016).

Dome Bogies Workshop.
VLT Paranal Presentation.
International conference SPIE (2016).

ESO Workshop Paranal.
Catastrophic failure, RTM 2 UT4, dismounted and replaced.
Repair Report (2017).

Fujfilm.
www.fujifilm.com/products/prescale/prescalefilm (2017).

Howard J., Meeks R., Ashby D., Davison W., Wiese J., Urban J., Hansen R., Schuh J.
Enclosure rotation on the Large Binocular Telescope.
Proc. SPIE 8444, Ground-based and Airborne Telescopes IV, 84443Y (2012).

Howieson D.
Vibration Monitoring; Envelope Signal Processing.
SKF Reliability Systems (2003).

https://www.engineeringtoolbox.com

https://www.fujifilm.com/products/prescale/prescalefilm

https://www.hecoinc.com/blog/electric-motor-ball-bearings-types-options

https://intertechnology.com/Kistler/pdfs/Accelerometer_Model_8152B.pdf

https://www.pcb.com/contentstore/docs/pcb_corporate/imi/products/manuals/603C01.pdf

https://www.skf.com/group/products/bearings-units-housings/roller-bearings/spherical-roller-bearings

Jamaludin N., Mba D., Bannister R.H. (2001).
Condition monitoring of low-speed rotating rolling element bearings using stress waves.
Journal of Process Mechanical Engineering, Institution of Mechanical Engineering.
Proceedings of the Institution of Mechanical Engineers 215 (E) (E4) (2001) 245-271.

Mathew J., Alfredson R.J.
The condition monitoring of rolling element bearings using vibration analysis.
J. Vibr., Acoust., Stress, and Reliab., 106 (3) (1984) 447-453.

Mathews J.R.
Acoustic Emission.
Gordon and Breach Science Publishers Inc.: New York, NY, USA (1983).

Mba D., Bannister R.H., Findlay G.E.
Condition monitoring of low-speed rotating machinery using stress waves: Parts I and II.
Proceedings of the Institution of Mechanical Engineers 213 (E) (1999) 153-185.

Mba D., Rao Raj B.K.N.
Development of acoustic emission technology for condition monitoring and diagnosis of rotating machines: bearings, pumps, gearboxes, engines and rotating structures.
Shock Vib. Dig. 38 (1) (2006) 3-16.

McFadden P.D.
Condition monitoring of rolling element bearings by vibration analysis.
Proceedings of IMechE Seminar on Machine Condition Monitoring, (1990) 49-53.

McFadden PD., Smith JD.
Vibration monitoring of rolling element bearings by the high frequency resonance technique – a review.
Tribol Int. 17 (1) (1984) 3-10.

Murga G, Bilbaoa A, Vizcargüenagaa A, Fernández A, Zarraoa A, Schneemann M.
Preliminary design for an enclosure for the European Extremely Large Telescope
Proc. SPIE 7012, Ground-based Airbone Telescopes II, 70121C (2008).

Palacio J.
RTM 5 UT4, dismounted, inspection and analysis.
ESO Test Report (2015).

Patel VM., Tandon N.
Vibration monitoring of very slow speed thrust ball bearings.
Conference Paper, ICSV20, Bangkok, (2013).

Randall RB., Antoni J.
Rolling Element Bearing Diagnostics--A Tutorial.
Mech. Syst. Sign. Process 25 (2) (2011) 485-520.

Rayo S.
Development of a method to determine the load distribution of the dome weight on the rotation mechanism of the Very Large Telescope of the Paranal Observatory.
Diploma Thesis, University of Concepción, Chile (2019).

Saavedra P.
Análisis de vibraciones mecánicas.
Notes of the subject “Analysis of Dynamical Systems”, Universidad de Concepción (2005).

SEBIS-1.
VLT Enclosures.
Document Number VLT-DWG-SEB-12300-0-260000-0001 (1994).

SEBIS-2.
VLT Enclosures.
Document Number VLT-DWG-SEB-12300-0-260102-0002_1v3 (1994).

SEBIS-3.
VLT Enclosures.
Document Number VLT-DWG-SEB-12300-0-260200-0001 (1994).

SEBIS-4.
VLT Enclosures.
Document Number VLT-TRE-SEB-12300-0013 (1994).

Shiroishi J., Li Y., Liang S., Kurfess T., Danyluk S.
Bearing condition diagnostics via vibration and acoustic emission measurements.
Mech. Syst. Sign. Process 11 (5) (1997) 693-705.

Tandon N., Nakra BC.
Detection of defects in rolling element bearings by vibration monitoring.
Indian J Mech Eng Div 73 (1993) 271-282.

BIBLIOGRAPHY

Budynas, R., Nisbett K. (2011).
Shigiley´s Mechanical Engineering Design.
Ninth Edition, McGraw-Hill.

Appendix A

Data sheets of the AE and ACC sensors

A.1 Kistler wideband sensor, Model 8152B11 for the AE measurements

Technical Data

Type	Unit	8152B111/121	8152B11/12sp
Sensitivity	dBref 1V/(m/s)	57	57
Frequency Range ±10dB	kHz	50 … 400	50 … 400
Ground Isolation	MΩ	>1	>1
Environmental:			
Shock Limit (0.5ms pulse)	gpk	2000	2000
Temperature Range Operating	°F	-40 … 140	-40 … 140
Output:			
Bias nom.	VDC	2.2	2.2
Impedance	Ω	<10	<10
Voltage full scale	V	±2	±2
Current	mA	2	2
Source:			
Voltage (Coupler)	VDC	5 … 36	5 … 36
Constant Current	mA	3 … 6	3 … 6
Construction:			
Sensing Element	type	ceramic	ceramic
Housing/Base	material	stainless steel	stainless steel
Sealing-housing/connector	type	hermetic	hermetic
Viton Cable Bend Radius, max.	in	0.6	0.6
Weight (without cable)	grams	29	29
Mounting Torque	lbf-in	80±10	80±10

(source: [https://intertechnology.com/Kistler/pdfs/Accelerometer_Model_8152B.pdf])

A.2 IMI vibration sensor, Model 603C01 for the ACC measurements

Model Number 603C01			
Performance	**ENGLISH**	**SI**	
Sensitivity(± 10 %)	100 mV/g	10.2 mV/(m/s²)	[2]
Measurement Range	± 50 g	± 490 m/s²	
Frequency Range(± 3 dB)	30 to 600,000 cpm	0.5 to 10,000 Hz	[3]
Resonant Frequency	1500 kcpm	25 kHz	[1]
Broadband Resolution(1 to 10,000 Hz)	350 µg	3434 µm/s²	[1]
Non-Linearity	± 1 %	± 1 %	[4]
Transverse Sensitivity	≤ 7 %	≤ 7 %	
Environmental			
Overload Limit(Shock)	5000 g pk	49,050 m/s² pk	
Temperature Range	-65 to +250 °F	-54 to +121 °C	
Temperature Response	See Graph	See Graph	[1]
Enclosure Rating	IP68	IP68	
Electrical			
Settling Time(within 1% of bias)	≤ 2.0 sec	≤ 2.0 sec	
Discharge Time Constant	≥ 0.3 sec	≥ 0.3 sec	
Excitation Voltage	18 to 28 VDC	18 to 28 VDC	
Constant Current Excitation	2 to 20 mA	2 to 20 mA	
Output Impedance	<150 ohm	<150 ohm	
Output Bias Voltage	8 to 12 VDC	8 to 12 VDC	
Spectral Noise(10 Hz)	8 µg/√Hz	78.5 (µm/s²)/√Hz	[1]
Spectral Noise(100 Hz)	5 µg/√Hz	49.1 (µm/s²)/√Hz	[1]
Spectral Noise(1 kHz)	4 µg/√Hz	39.2 (µm/s²)/√Hz	[1]
Electrical Isolation(Case)	$>10^8$ ohm	$>10^8$ ohm	
Physical			
Size (Hex x Height)	11/16 in x 1.65 in	18 mm x 42.2 mm	
Weight	1.8 oz	51 gm	
Mounting Thread	1/4-28 Female	No Metric Equivalent	[5]
Mounting Torque	2 to 5 ft-lb	2.7 to 6.8 N-m	
Sensing Element	Ceramic	Ceramic	
Sensing Geometry	Shear	Shear	
Housing Material	Stainless Steel	Stainless Steel	
Sealing	Welded Hermetic	Welded Hermetic	
Electrical Connector	2-Pin MIL-C-5015	2-Pin MIL-C-5015	
Electrical Connection Position	Top	Top	

(source: [https://www.pcb.com/contentstore/docs/pcb_corporate/imi/products/manuals/603C01.pdf])

Appendix B

UT2-RTM3, bearing 1, analysis period: 40 s to 61 s

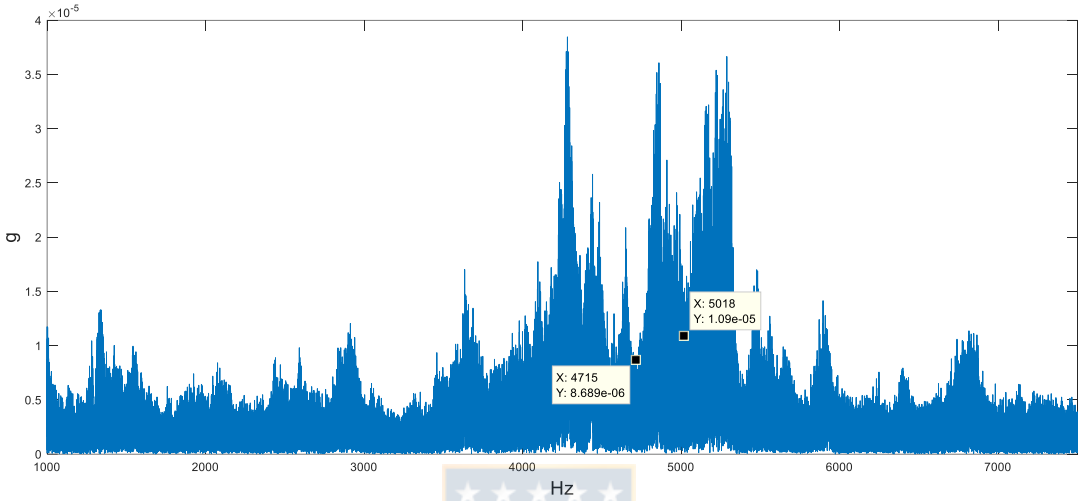

ACC-H high frequency spectrum with filter range example (center frequency: 4867 Hz).

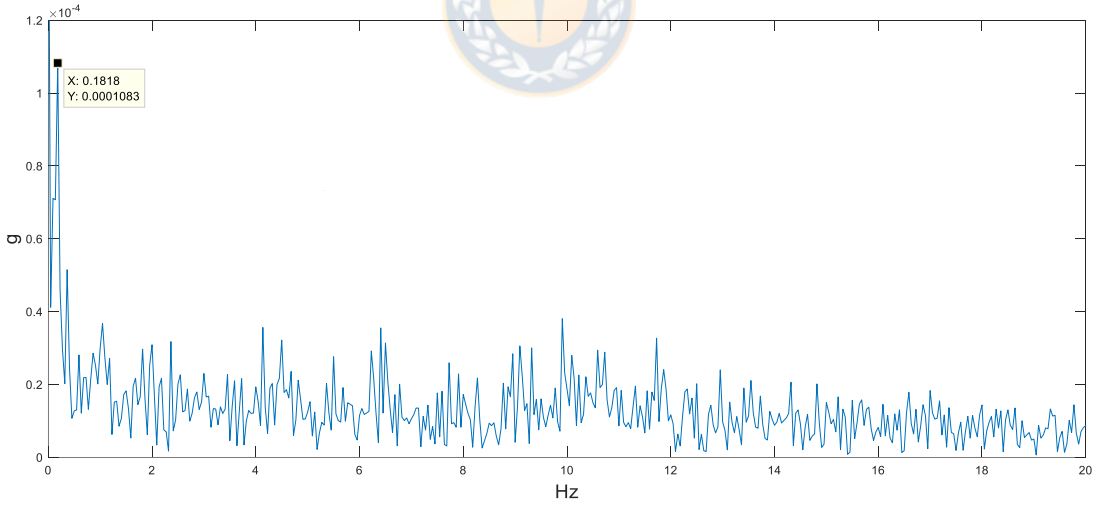

Filtered ACC-H envelope spectrum (center frequency: 4867 Hz).